Title
Magnetic Memory with Antiferromagnets and Multilayers

Author
Barra, Anthony

Publication Date
2019

Peer reviewed|Thesis/dissertation

UNIVERSITY OF CALIFORNIA

Los Angeles

Magnetic Memory with Antiferromagnets and Multilayers

A dissertation submitted in partial satisfaction of the
requirements for the degree Doctor of Philosophy
in Mechanical Engineering

by

Anthony Barra

2019

ABSTRACT OF THE DISSERTATION

Voltage-Controlled Magnetic Memory with Antiferromagnets and Multilayers

by

Anthony Barra

Doctor of Philosophy in Mechanical Engineering
University of California, Los Angeles, 2019
Professor Gregory P. Carman, Chair

In the next 10 years, the demand for data storage will increase exponentially until current storage methods are economically untenable. The speed and energy efficiency of digital memory will need to be improved by at least a factor of 100-10,000 times. Magnetic memory offers a major energy efficiency improvement (> 100 times) because it can be integrated with voltage-controlled switching methods, like multiferroicity (i.e. strain-coupling), but it is also unfortunately speed limited by the material's ferromagnetic resonance. To surpass the speed limit, ferromagnetic materials can be substituted by magnetic multilayers or antiferromagnets, since their resonances are 10-1000 times higher. However, further work is required to integrate these under-studied materials into the necessary highly energy efficient multiferroic control schemes. In this dissertation, three main problems are addressed regarding voltage control of multilayers and antiferromagnets. First, the level of exchange coupling and magnetic property averaging in multilayers is not well understood. In this dissertation, a novel micromagnetic simulation of a multilayer is presented that includes a distinct multilayer exchange coupling term, and the model's predictions are compared to experimental magnetic depth profiles obtained via neutron scattering.

Second, a deficiency in the literature regarding strain control of antiferromagnets is corrected by presenting a new antiferromagnetic magneto-electro-mechanical model that predicts both near THz and aJ-level energy costs for switching. Finally, the first experimental test to measure strain-induced anisotropy in antiferromagnets is presented, showing that small strains (around 300 με) produces magnetoresistance changes similar to those observed when 3 Tesla of external magnetic field is applied. This work should provide new pathways to simulate and integrate next-generation materials choices into magnetic memory.

The dissertation of Anthony Barra is approved.

Robert N. Candler

Christopher S. Lynch

Kang Lung Wang

Gregory P. Carman, Committee Chair

University of California, Los Angeles

2019

For my parents, Anthony G. and Kristen Barra

Table of Contents

List of Figures

ACKNOWLEDGEMENTS

This material is based upon work supported by or in part by the U.S. Army Research Laboratory and the U.S. Army Research Office under Grant No. W911NF-17-0364. This work is also supported by the NSF Nanosystems Engineering Research Center for Translational Applications of Nanoscale Multiferroic Systems under the Cooperative Agreement Grant No. EEC-1160504 and, in part, by FAME, one of the six centers of STARnet, a Semiconductor Research Corporation program sponsored by MARCO and DARPA.

VITA

Education

2014 M.S., Mechanical Engineering
Columbia University in the City of New York, New York, NY, USA

2012 B.A., Physics
University of Southern California, Los Angeles, CA, USA

2012 B.S., Business Administration
University of Southern California, Los Angeles, CA, USA

Employment History

2014-2019 Graduate Student Researcher
University of California, Los Angeles, CA, USA

SELECTED PUBLICATIONS AND CONFERENCE PRESENTATIONS

Barra, A., et al. (2019). Voltage-Induced Anisotropy Changes in Polycrystalline NiO/Pt Measured by Spin Hall Magnetoresistance. Manuscript under preparation.

Jamer, M.E., […], Barra, A., et al. (2018). Long Range Electric Field Control of Permalloy Layers in Strain-Coupled Composite Multiferroics. *Physical Review Applied 10* (4), 044045.

Barra, A., et al. (2018). Voltage Control of Antiferromagnetic Phases at Near-Terahertz Frequencies. *Physical Review Applied 9* (3), 034017.

Barra, A. et al. (2017). Near THz Voltage Control of Antiferromagnetism. Oral presentation at the Magnetism and Magnetic Materials (MMM) Conference, Pittsburgh, PA, USA.

Navabi, A., […], Barra, A. et al. (2017). Efficient Excitation of High-Frequency Exchange-Dominated Spin Waves in Periodic Ferromagnetic Structures. *Physical Review Applied 7* (3), 034027.

Wang, Q., […], Barra, A. et al. (2017). Strain-Mediated 180 Switching in CoFeB and Terfenol-D Nanodots with Perpendicular Magnetic Anisotropy. *Applied Physics Letters 110* (10) 102903.

Chen, C., […], Barra, A. et al. (2017). Voltage Induced Mechanical/Spin Wave Propagation Over Long Distances. *Applied Physics Letters 110* (7) 072401.

I. Introduction

1.1 Motivation

There is a need to immediately and massively improve the speed and energy efficiency of data storage. Most modern data storage mediums rely on current-mediated charge transfer in complimentary metal-oxide-semiconductor (CMOS) transistors, a process that is limited to GHz speeds and is only about 0.0003% efficient [1]. These poor performance metrics have generally been deemed acceptable because the total amount of power used for data storage on most computing platforms is relatively low, at less than 4% of the total [2], and the transfer of large files (> 1 Gigabyte) is rare. Since there are other major power users and performance bottlenecks, like the central processing unit (CPU), the graphics processing unit (GPU), and the display (particularly for smart phones and tablets), those areas have garnered more attention for improvement in recent years.

However, a major shift is underway that will create a totally new demand for data, and the total amount of data needing to be stored will increase dramatically in the next 10 years. This is due to machine learning, and in particular deep learning, which allows computers to do algorithm-based inferential learning that requires little or no intervention from a user. These methods are used in self-driving cars, advanced facial recognition, and interpretation of spoken language, just to name a few [3]. The main input required to perform machine learning is curated data about the task being learned. In particular, these algorithms often need hundreds of millions, or billions, of data points to learn from. As the number and uses of machine learning proliferate, the requirement to store data will grow substantially. Today, more data is generated every 2 years than in all of prior human history [4], and the energy cost of data centers seems to double every 5 years. [5].

If this trend continues, it would have an untenable environmental and economic impact. To avoid this, the poor efficiency and GHz speed limitation of data storage, particularly in the form of digital information storage on hard drives, will need to be improved by a factor of hundreds or thousands of times.

The best way to make such an improvement is by removing the reliance on electrical charge (i.e. current) as a data storage medium. The equation dictating power dissipation in electrical devices states that this would drastically improve energy efficiency because the dissipated power scales with the square of the operating current. To avoid using current may require abandoning CMOS-based memory entirely.

One promising option is to substitute electrical devices by spin or magnetism-based alternatives. In these devices, information would be carried by the electron's spin, which can be propagated over long distances (centimeters) with very low signal loss [6] and with almost no intrinsic heating [7]. Another advantage is that magnetism-based systems can store non-volatile information, meaning the device's power can be turned off and the data remains stored [8].

To pursue this magnetic option, the main requirement is to integrate the magnetic memory read and write operations (i.e. to record digital bits, 1's and 0's) without electrical current, in a manner that is both energy efficient and high speed. For commercial applicability, it would be optimal not to sacrifice memory bit density either.

Under all of these restrictions, the best-known method is to include the magnetic memory bits into two-phase multiferroic composites, where the magnetic layers are deposited on top of a piezoelectric substrate. This would allow out-of-plane electric fields in the piezoelectric layer to generate in-plane strains that are sufficient to rotate the magnetization of the top layer through

magnetostrictive coupling [9]. The main benefit of this approach is that actuation of the piezoelectric layer is voltage controlled, meaning that the power dissipation is extremely low, approaching attojoules per state switch at the theoretical limit [1] (100-1000 times better than CMOS state-of-the-art [1]). A secondary benefit is that the total required power also scales favorably with shrinking device area, making it an optimal choice for high density memory.

Despite the ultralow energy cost of this approach, one major limitation is the device speed. Since most multiferroics include ferromagnetic materials as the top layer, they are speed limited by the material's native ferromagnetic resonance frequency (FMR), which is similar to the low GHz speeds available with the older CMOS technology.

To further speed up magnetic memory, the material properties themselves need to be changed. One option is to layer different magnetic materials with desirable properties into thin film stacks until the composite behavior becomes an average of the constitutive films. This has the benefit that standard magnetic metrology tools (superconducting quantum interference device (SQUID), Kerr microscopy, etc.) can still be used to characterize the stack, but the range of potential material property changes are limited. A more radical approach is to change the class of the magnetic material entirely, offering substantial changes, but this may complicate characterization of the memory read and write processes.

If the multilayer stack approach is used, the goal would be to combine dissimilar materials with unique features so that the composite expresses both features at levels not possible in a single material. In a memory context, the best possible case would be to combine high magnetoelasticity materials with low dissipation (i.e. low damping and magnetically soft) materials to create a composite that is both magnetoelastic but energy efficient. Despite the common use of layering in

magnetic memory (e.g. for spin polarization or exchange biasing), the extent to which the layers actually couple and average their material properties remains unknown.

If the class of magnet is instead substituted entirely, it would be beneficial to replace the ferromagnetic layer with an antiferromagnet. Antiferromagnets exhibit an internally canceling magnetization that results in high resonances (100 GHz – 10 THz) and resistance to external magnetic fields. These materials are not well studied and, consequently, their magnetoelastic coefficients are rarely known. In addition, their lack of moment makes both reading and writing their magnetic state difficult and an open area of research.

In this dissertation, both multilayer stacks and antiferromagnets are examined for incorporation into multiferroic memory. First, they are studied at the device level using a combination of theory and experiment, and then factors related to their use in magnetic memory are identified. Specifically, a candidate system containing low dissipation NiFe and high magnetostriction CoFeB multilayers are studied via micromagnetic modeling and polarized neutron beam reflectometry to examine the level of magnetic property averaging and coherent rotation between the layers. Then, a novel antiferromagnetic multiferroic memory is proposed and analyzed in two parts. In part one, the device operation is simulated using a magnetomechanical finite element model. In part two, the model is used to design a single-bit NiO/Pt test device, whose magnetoresistance is characterized to prove the feasibility of these materials for future use.

1.2 Dissertation Overview

The goal of this dissertation is to address two major shortcomings in the multiferroic literature. Namely, it is difficult to incorporate either (i) multilayer magnetic stacks or (ii) antiferromagnets in multiferroic memory due to insufficient modeling methods and a lack of feasibility studies. This

dissertation seeks to correct these issues by providing both novel micromagnetic modeling methods and proof-of-concept feasibility studies in simplified devices. For multilayer stacks, NiFe/CoFeB is used as a test-bed to study the presence of interlayer coupling and magnetic property averaging. For antiferromagnets, polycrystalline NiO is examined as a candidate strain-mediated memory material with magnetoresistive read-out.

The contents of the dissertation are as follows: Chapter 2 provides a review of the fundamental physics and literary history surrounding strain-mediated multiferroic memory, specifically as it concerns multilayers and antiferromagnets. Chapter 3 presents the candidate NiFe/CoFeB multilayer stack, the newly developed micromagnetic analyses used to study it, and the neutron reflectometry results that validate the simulations. Chapter 4 includes the first fully-coupled magnetomechanical simulation of an antiferromagnet in a memory context. This model is then applied in Chapter 5 to design a NiO/Pt test-bed with magnetoresistive read-out that exhibits the first-ever measurements of strain-induced anisotropy changes in a polycrystalline antiferromagnet.

1.3. Chapter References

[1] Wang, K. L., J. G. Alzate, and P. Khalili Amiri. "Low-power non-volatile spintronic memory: STT-RAM and beyond." *Journal of Physics D: Applied Physics* 46.7 (2013): 074003.

[2] Carroll, Aaron, and Gernot Heiser. "An Analysis of Power Consumption in a Smartphone." *USENIX annual technical conference*. Vol. 14. 2010.

[3] Jordan, Michael I., and Tom M. Mitchell. "Machine learning: Trends, perspectives, and prospects." *Science* 349.6245 (2015): 255-260.

[4] S. Sagiroglu and D. Sinanc, “Big data: a review”, in Collaboration technologies and systems (cts), 2013 international conference on (IEEE, 2013), pp. 42–47.

[5] Koomey, Jonathan G. "Worldwide electricity used in data centers." *Environmental research letters* 3.3 (2008): 034008.

[6] Cornelissen, L. J., et al. "Long-distance transport of magnon spin information in a magnetic insulator at room temperature." *Nature Physics* 11.12 (2015): 1022.

[7] Hong, J., et al. "Experimental verification of Landauer's principle in erasure of nanomagnetic memory bits." *arXiv preprint arXiv:1411.6730* (2014).

[8] Wang, K. L., and P. Khalili Amiri. "Nonvolatile spintronics: perspectives on instant-on nonvolatile nanoelectronic systems." *Spin*. Vol. 2. No. 02. World Scientific Publishing Company, 2012.

[9] Cui, Jizhai, et al. "A method to control magnetism in individual strain-mediated magnetoelectric islands." *Applied Physics Letters* 103.23 (2013): 232905.

II. Background

2.1. Magnetism and Magnetic Memory

Memory, in a computing context, serves two basic functions. It must retrieve recorded information and record new information as ordered by the CPU. This is referred to as “reading” and “writing” to the memory.

In magnetic memory, the information is encoded into a material’s magnetic states by controllably remagnetizing it. Normally the data consists of binary 1’s and 0’s, so it is natural to store the data into two opposing magnetic states, which can be thought of as “up” or “down”. In order to keep the states separated, magnetic memories often physically distinguish each recording element (or memory bit) either by patterning them into 2-dimensional arrays or writing to individual domains

within a larger magnetic domain structure (as in credit cards or magnetic tape recorders). Since "reading" and "writing" are the basic functions of the memory, numerous methods have been developed for manipulating or identifying localized (micron-scale or smaller) magnetic states.

There are many possible read mechanisms, but most common commercial magnetic memories rely on either stray field reading or resistance change identification. In the first method, a magnetic bit is passed at some speed by a wire loop, and its demagnetizing field (which travels through the air) induces a current in the loop. The sign of the current can then be corresponded to the "up" or "down" magnetization state at the location of the loop. A second method relies on magnetoresistance, or a magnet's change in electrical resistance when its magnetization state changes. In this case, changing the magnetization creates changes in the spin-dependent electron density of states, resulting in high resistance in one magnetization state and low resistance in the other (with maximal change occurring when the two states are 180˚ apart). There are many forms of magnetoresistance, like anisotropic magnetoresistance (AMR), giant magnetoresistance (GMR), and tunneling magnetoresistance (TMR), but their descriptions can be found elsewhere [1].

Writing, alternatively, always proceeds by applying a magnetic field to switch a bit. The applied field can either be external, like those applied by an electromagnet, or derived from complex coupling or internal effects. In the latter case, the applied field can often be expressed as a function of a non-magnetic variable and is thus referred to as an "effective field". Both external field and effective field writing methods are common. Spinning disk hard-drives, for example, used the wire loop read head for writing by passing a current through it [2]. However, as mentioned in the Introduction above, since this method relies on current generation, it is very inefficient and does not scale favorably to small device size. As a result, the most advanced magnetic memories of

today are pursuing effective field alternatives. Some popular effective-field switching methods are spin transfer torque (STT) [3], spin-orbit torque (SOT) [4], and heat-assisted magnetic recording (HAMR) [5]. In the first two methods, current passes through an adjacent magnetic layer (STT) or heavy metal layer (SOT) instead of an electromagnet, and these adjacent layers transfer spin momentum by shifting the electron density of states. Alternatively, HAMR works to elevate a bit's energy level with a laser so that it is easier to switch. While these methods offer performance benefits like individual bit addressability at the nanoscale, neither is substantially faster or more energy efficient.

For this reason, significant attention has been focused on leveraging magnetoelastic coupling to do effective field switching.

2.2. Magnetoelasticity

The theory of magnetoelasticity states that straining a magnetic material can change its effective magnetic field, and that changing its effective magnetic field can, in turn, change its strain. In the small strain limit, the theory connecting magnetoelastic strain, ε_{ij}^{ME}, and effective magnetoelastic field, H_{ME}, is linear, and follows [6]

$$H_{ME} = \frac{-2}{\mu_0 M_S}(B_1 \varepsilon_{ii}^{total} m_i + \sum_{j \neq i} B_2 \varepsilon_{ij}^{total} m_j)$$

$$\varepsilon_{ij}^{ME} = \frac{3}{2}\lambda_s(m_i m_j - \frac{1}{3})$$

where B_1 and B_2 are the magnetoelastic coefficients, λ_s is the saturation magnetostriction, $\boldsymbol{m}$ is the magnetization, and the total strain $\boldsymbol{\varepsilon^{total}}$ is comprised of the magnetoelastic strain $\boldsymbol{\varepsilon^{ME}}$ and strain from other sources $\boldsymbol{\varepsilon^{other\ sources}}$.

This effect was originally discovered in iron by James Prescott Joule in 1842, however he judged the effect to be so small that it was irrelevant [7]. As a result, the effect was largely ignored until the discovery of materials with large magnetostriction, namely those containing dysprosium, like $TbDyFe_2$ (Terfenol-D), in the 1970's [8][9]. Since then, the discovery of new magnetoelastic materials has slowed and, crucially, has been focused almost exclusively on ferromagnetic materials, neglecting the multilayer composites and antiferromagnetic materials of interest in this dissertation.

There are currently no commercially available magnetostriction-operated magnetic memories, but they have received substantial attention in the scientific literature [10][11][12]. Most of the magnetostriction-based memories utilize a multiferroic composite structure for strain control, so the development of this technology is discussed in the following section.

2.3. Multiferroics and Strain-Controlled Magnetic Memory

Multiferroics are a class of material that exhibit three-way coupling between electric field, strain, and magnetic state. The original multiferroic materials, like Cr_2O_3 (discovered in 1961 by D.N. Astrov [13]), were of the intrinsic type, meaning that the materials exhibited the three-way coupling in a single-phase. Other popular modern intrinsic multiferroics include BFO [14] and CFO [15], which have garnered attention as potential memory materials for both their magnetostrictive and magnetoelectric properties. Despite this interest, this dissertation will focus largely on two-phase multiferroics since they exhibit larger three-way coupling and are more relevant for technological applications.

Two-phase multiferroics are composites between magnetoelastic materials and piezoelectric materials. The concept is that by layering the most magnetoelastic and piezoelectric materials

together, one can the maximize the joint magnetoelastic effect. This can be thought of as a two-step process; one that converts electric field into strain and one that converts strain into magnetic changes. Mathematically, this can be represented by

$$\frac{dM}{dE} = \frac{dM}{d\varepsilon} \times \frac{d\varepsilon}{dE}$$

where E is electric field, ε is the strain, and M is the magnetization, making $\frac{dM}{d\varepsilon}$ and $\frac{d\varepsilon}{dE}$ the magnetoelastic and piezoelectric coefficients, respectively.

The idea to combine these materials in this way was initially put forth by Ryu et al. in two papers in 2001 and 2002 [16][17], with the highest reported magnetoelectricity coming from Terfenol-D/PMN-PT laminate composites [16] of bulk materials. Since then, the landscape of available materials has exploded, and the convenience and high performance has lead to their widespread investigation as platforms for magnetoelastic-operated magnetic memory.

While Ryu et al. initially focused on bulk measurements, by the mid-2000's the focus had shifted to characterizing magnetic switching in thin films, since these were more technologically relevant in the burdgeoning MEMS era [18]. In this case, electric field was applied across the entire substrate, and the average magnetic response of the surface magnetic film was measured via standard magnetic metrology tools. Later, the films were substituted by patterned magnetic nanoelement arrays including Ni [19] and the magnetic tunnel junction material CoFeB [20]. In early forms of these geometries the entire substrate is strained, meaning that the entire nanoelement array would (at least theoretically) experience the same strain-induced anisotropy. However, straining entire arrays at once is uninteresting in a memory context, since the bits need to be individually addressable to build a memory.

As a result, recent focus has shifted to designing and fabricating magnetic nano-islands that can be strained individually. This incorporated design, fabrication, and testing work. The concept was initially reported by J. Cui, et al. in 2013 [19], where they showed a coercive field shift in a 35 nm-thick Ni dot under strain. With the concept proven, there was a need to develop tools to engineer complete devices, taking into account factors like nano-island size, shape, and strain effects. This was accomplished by C. Y. Liang, et al. in 2014, in a series of two papers [20][21] that developed a fully-coupled piezoelectric-elastodynamic-magnetodynamic finite element analysis (FEA) package. Full details of his model are available in other dissertations [22][23], and involve formulation of the micromagnetic Landau-Lifshitz-Gilbert equation [24] in weak form. The model predicted that switching is possible, and this was later validated experimentally by J. Cui in 2015 [25]. Cui controlled the onion-state domains of Ni nano-rings using strain and imaged

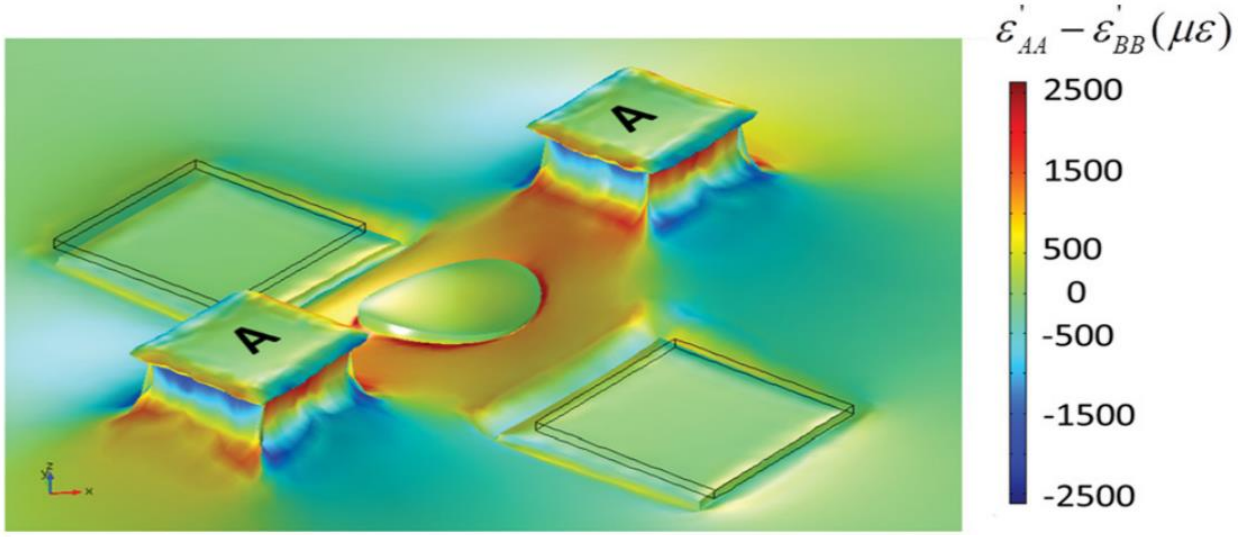

Figure 2.1 – C.Y. Liang's finite element simulation [21] showing the strain-state of a multiferroic composite under applied electric fields at electrodes A.

the switched states via magnetic force microscopy. However, all of these results only address 90˚ in-plane switching, which is less interesting for memory because the corresponding resistance changes are low and the device footprint is too large. For this reason, there was a significant push

towards 180˚ out-of-plane switching, which is difficult to accomplish with strain because the strain effect is uniaxial and confined to the two in-plane axes of the substrate. Despite this, a method for 180˚ out-of-plane switching was proposed and theoretically examined by X. Li [26], also in 2015. Her approach combined perpendicular magnetic anisotropy (PMA), which yields an out-of-plane easy axis, with "ballistic switching" – a method that uses strain to switch from out-of-plane to in-plane, and then times the strain release to carry the magnetization over to the opposing easy axis direction. While this method works in theory, it has not been tested comprehensively, and may face poor writing success rates due to the nanosecond timing requirements associated with the strain release.

Until this dissertation, none of the modeling approaches presented here have been developed for materials other than ferromagnets and, as a result, no devices have been tested that were designed the same way. As previously mentioned, the ability to model and include other materials would greatly expand the potential of this multiferroic strain-control method. The next two sections discuss the progress that has been made concerning multilayers and antiferromagnets in magnetic memory.

2.4. Multilayers

Multilayers consist of stacked thin films of different magnetic materials that, depending on their thicknesses, may exhibit properties that vary greatly from the constituent films. This opens many possibilities for improved performance, but such benefits come at the cost of more difficult device design and experimental interpretation.

Whereas the previous section outlined a full strain-coupled modeling approach for ferromagnets, no widely available code exists for simulating even the isolated micromagnetic dynamics of

multilayers. This creates significant problems for understanding how different layers in a stack interact. In the small thickness limit (usually defined by the exchange length $l_{ex} = \sqrt{\frac{2A_{ex}}{\mu_0 M_S^2}}$ [23], where A_{ex} is the material's exchange constant), it is generally accepted that layered films are fully magnetically coupled. However, at larger thicknesses, it becomes unclear whether the interfacial exchange coupling or demagnetizing effects dominate the relative magnetizations of the two layers. It is known that the interfacial exchange coupling is likely to dominate within the first few nanometers adjacent to the interface (as can be inferred from quantum mechanics), but it is not known whether that effect is transferred to the stack's top and bottom by the intra-layer exchange interaction.

Despite these difficulties, multilayers are still commonly used in many magnetic devices, including in memory. For example, TMR relies on CoFe/CoFeB free and pinned layers in magnetic tunnel junctions (MTJs) both for memory and sensing applications [27]. However, it is uncommon to see thicker multilayers for the reasons previously mentioned.

One new area of research that is outside the scope of this dissertation but worth mentioning is the combination of materials with opposite signs of magnetostriction. This would enable stacks of magnetic layers that stagger their magnetization by 90 degrees under strain application, and have some critical strain at which the layers decouple [28].

2.5. Antiferromagnetism

The fundamental physics of antiferromagnetism was initially described by Louis Néel in the 1930's and 40's – work that earned him the Nobel prize in Physics in 1970 [29]. He described them as magnetic materials that exhibit no magnetic moment, a property that made them resistant to interaction with external electromagnetic fields or materials. For this reason, he judged in his

Nobel lecture that antiferromagnets were “extremely interesting from a theoretical viewpoint, but do not seem to have any applications”.

In general, antiferromagnets are separated into categories based on their spin structure. There are either collinear or non-collinear antiferromagnets. Collinear ones exhibit same-sized magnetic moments that cancel by pointing 180˚ apart, and non-collinear ones exhibit more complicated spin structures wherein canceling takes place between 3 or more moments of varying magnitudes and angles.

This canceling moment endows antiferromagnets with a number of unique properties that are promising for memory applications:

(i) First, they largely do not respond to small applied fields, usually anything less than 1 Tesla. If fields are applied above this threshold, the moments begin to cant relative to one another, resulting in a small moment that is perpendicular to the direction of magnetic alignment (the so-called Néel vector). If the applied field is large enough, the canted moment can rotate the sublattices perpendicular to the applied field; this is referred to as a “spin flop” transition. Above 2-3 Tesla (but usually closer to 7+ Tesla), the external field can overcome the antiferromagnetic exchange coupling and rotate all the moments in the direction of the field; this is the “spin flip” transition. After the spin flip transition, the antiferromagnet is magnetically saturated. Compared to ferromagnets, the saturating fields of antiferromagnets are 100-10,000 times higher. In a memory context, this means that antiferromagnets are resilient to magnetic noise [6].

(ii) Second, the presence of an additional (i.e. more than one) magnetic sublattice in antiferromagnets increases their resonance frequencies to near the THz range. The reason for this is that antiferromagnetic resonance is mediated predominantly by the

antiferromagnetic exchange field H_{ex} instead of the general anisotropy field H_a, as in ferromagnets. Since the antiferromagnetic exchange field is very high (often in the 10s or 100's of Tesla [30]), the resonances are correspondingly high, as can be calculated from the resonance equation [30], which follows

$$\omega_0 = \gamma\mu_0\sqrt{H_a(H_a + 2H_{ex})}$$

where $\gamma\mu_0$ is a material-dependent constant converting field to frequency, and ω_0 is the resonance frequency. In a memory context, the possibility for high frequencies means a chance

(iii) Third, the lack of moment in antiferromagnets also results in a lack of stray magnetic field since the demagnetization energy is near zero. This enables antiferromagnetic memory bits to be packed more densely in arrays since there is no device-to-device magnetic cross-talk [31].

Despite these promising qualities, the scope of research on antiferromagnets for use in memory is limited.

Originally, antiferromagnets were investigated only as a means to control ferromagnets, namely through exchange biasing, where ferromagnets are layered with antiferromagnets to shift the center of the ferromagnet's M-H loop either up or down in field [32]. This has been used extensively as a means of creating local on-chip magnetic pinning in the fixed layers of MTJ memory [27]. However, in these systems, the antiferromagnet is never switched, and thus exchange biasing is not a contributing factor in either the reading or writing steps of the memory.

The earliest on-chip antiferromagnet memories (i.e. those where the antiferromagnet itself was the information-carrying layer) used an SOT writing mechanism developed by X. Marti et al. [33],

with AMR read-out. They developed a tetragonal phase of CuMnAs (with P. Wadley et al. [34]) that generates its own SOT during unpolarized current application due to crystalline asymmetry. However, the method requires a complex materials growth process, and only offers low resistance changes between written states, so this method has seen limited use. A secondary writing method involves laser-induced optical torques [35], but does not scale well to large memory bit arrays.

As previously mentioned, this dissertation focuses on using magnetostriction as an alternative to either SOT or optical writing methods. So far, this concept has received little attention. The potential for strain to change the magnetoresistance properties of antiferromagnets was first observed in 2014 in $La_{0.4}Sr_{0.6}MnO_3$ (LSMO), where strains induced by large film-to-substrate lattice mismatches resulted in 55% enhancement of AMR [36]. Similar strain-induced effects were also reported in 2017 for Mn_2Au, as measured by x-ray magnetic linear dichroism (XMLD) [37]. However, both reports do not address tunable straining. To address this, more recent work has included antiferromagnets in multiferroic composites. This has only been done twice, for MnPt [38] and Mn_2Au [39]. Of these, only the MnPt paper focused on magnetoresistive Néel vector read-out (by TMR). The Mn_2Au paper, alternatively, only focuses on tunable exchange biasing.

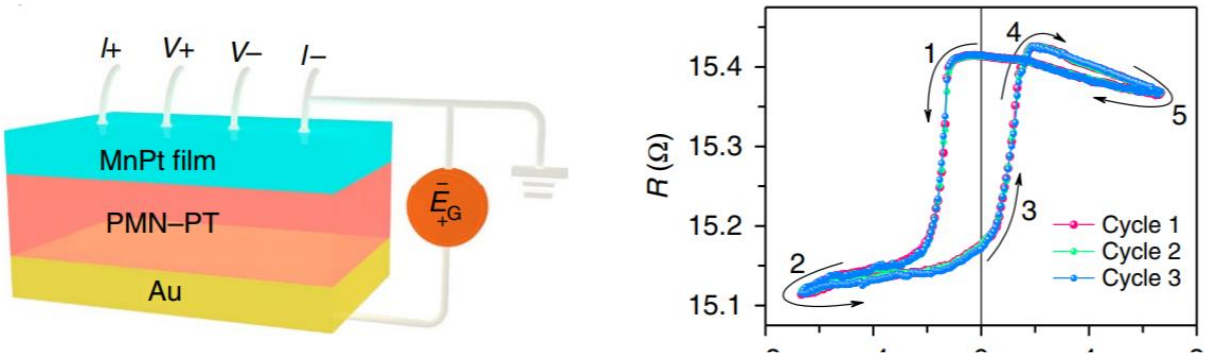

Figure 2.2 – (Left) The thin-film MnPt multiferroic composite structure studied by Yan et al., [38] highlighting the 4-point resistance measurement arrangement. (Right) The measured surface resistance of the MnPt under applied voltage-induced strain. The hysteresis indicates repolarization of the substrate.

Both papers rely on Néel vector switching that occurs only for complete repolarization of the piezoelectric layer, meaning that the results are not applicable for individual bit addressing or high speed opration.

2.6 Chapter References

[1] Bhatti, Sabpreet, et al. "Spintronics based random access memory: a review." *Materials Today* 20.9 (2017): 530-548.

[2] Hylick, Anthony, et al. "An analysis of hard drive energy consumption." *2008 IEEE International Symposium on Modeling, Analysis and Simulation of Computers and Telecommunication Systems*. IEEE, 2008.

[3] Wang, K. L., J. G. Alzate, and P. Khalili Amiri. "Low-power non-volatile spintronic memory: STT-RAM and beyond." *Journal of Physics D: Applied Physics* 46.7 (2013): 074003.

[4] Garello, Kevin, et al. "Ultrafast magnetization switching by spin-orbit torques." *Applied Physics Letters* 105.21 (2014): 212402.

[5] Rottmayer, Robert E., et al. "Heat-assisted magnetic recording." *IEEE Transactions on Magnetics* 42.10 (2006): 2417-2421.

[6] Barra, Anthony, et al. "Voltage Control of Antiferromagnetic Phases at Near-Terahertz Frequencies." *Physical Review Applied* 9.3 (2018): 034017.

[7] Joule, James Prescott. "XVII. On the effects of magnetism upon the dimensions of iron and steel bars." *The London, Edinburgh, and Dublin Philosophical Magazine and Journal of Science* 30.199 (1847): 76-87.

[8] Clark, A. E., B. F. DeSavage, and R. Bozorth. "Anomalous thermal expansion and magnetostriction of single-crystal dysprosium." *Physical Review* 138.1A (1965): A216.

[9] Abbundi, R., and A. Clark. "Anomalous thermal expansion and magnetostriction of single crystal Tb. 27 Dy. 73 Fe 2." *IEEE Transactions on Magnetics* 13.5 (1977): 1519-1520.

[10] Scott, J. F. "Data storage: Multiferroic memories." *Nature materials* 6.4 (2007): 256.

[11] Bibes, Manuel, and Agnès Barthélémy. "Multiferroics: Towards a magnetoelectric memory." *Nature materials* 7.6 (2008): 425.

[12] Hu, Jia-Mian, et al. "Electric-field control of strain-mediated magnetoelectric random access memory." *Journal of Applied Physics* 107.9 (2010): 093912.

[13] Astrov, D. N. "Magnetoelectric effect in chromium oxide." *Sov. Phys. JETP* 13.4 (1961): 729-733.

[14] Chu, Y-H., et al. "Nanoscale domain control in multiferroic BiFeO3 thin films." *Advanced Materials* 18.17 (2006): 2307-2311.

[15] Ortega, N., et al. "Dynamic magneto-electric multiferroics PZT/CFO multilayered nanostructure." *Journal of materials science* 44.19 (2009): 5127-5142.

[16] Ryu, Jungho, et al. "Effect of the Magnetostrictive Layer on Magnetoelectric Properties in Lead Zirconate Titanate/Terfenol-D Laminate Composites." *Journal of the American Ceramic Society* 84.12 (2001): 2905-2908.

[17] Ryu, Jungho, et al. "Magnetoelectric effect in composites of magnetostrictive and piezoelectric materials." *Journal of electroceramics* 8.2 (2002): 107-119.

[18] Eerenstein, Wilma, N. D. Mathur, and James F. Scott. "Multiferroic and magnetoelectric materials." *nature* 442.7104 (2006): 759.

[19] Cui, Jizhai, et al. "A method to control magnetism in individual strain-mediated magnetoelectric islands." *Applied Physics Letters* 103.23 (2013): 232905.

[20] Liang, Cheng-Yen, et al. "Modeling of magnetoelastic nanostructures with a fully coupled mechanical-micromagnetic model." *Nanotechnology* 25.43 (2014): 435701.

[21] Liang, Cheng-Yen, et al. "Electrical control of a single magnetoelastic domain structure on a clamped piezoelectric thin film—analysis." *Journal of Applied Physics* 116.12 (2014): 123909.

[22] Chavez, Andres Cornel. *Voltage Control of Magnetism in Nanoscale Artificial Multiferroics*. Diss. UCLA, 2018.

[23] Kundu, Auni Aunnoyee. *Multiferroics for Future Cell Sorting Devices*. Diss. UCLA, 2019.

[24] Szambolics, H., et al. "A constrained finite element formulation for the Landau–Lifshitz–Gilbert equations." *Computational Materials Science* 44.2 (2008): 253-258.

[25] Cui, Jizhai, et al. "Generation of localized strain in a thin film piezoelectric to control individual magnetoelectric heterostructures." *Applied Physics Letters* 107.9 (2015): 092903.

[26] Li, Xu, et al. "Strain-mediated 180 perpendicular magnetization switching of a single domain multiferroic structure." *Journal of Applied Physics* 118.1 (2015): 014101.

[27] Freitas, Paulo P., Ricardo Ferreira, and Susana Cardoso. "Spintronic sensors." *Proceedings of the IEEE* 104.10 (2016): 1894-1918.

[28] Xiao, Zhuyun, et al. “Tunable magnetoelastic effect in voltage-controlled exchange-coupled composite multiferroic microstructures”. In preparation. 2019.

[29] Neel, Louis. "Magnetism and the local molecular field." *Nobel Prize Lecture* (1970).

[30] Coey, John MD. *Magnetism and magnetic materials*. Cambridge university press, 2010.

[31] Lebrun, R., et al. "Tunable long-distance spin transport in a crystalline antiferromagnetic iron oxide." *Nature* 561.7722 (2018): 222.

[32] Nogués, Josep, et al. "Exchange bias in nanostructures." *Physics reports* 422.3 (2005): 65-117.

[33] Marti, X., et al. "Room-temperature antiferromagnetic memory resistor." *Nature materials* 13.4 (2014): 367.

[34] Wadley, P., et al. "Tetragonal phase of epitaxial room-temperature antiferromagnet CuMnAs." *Nature communications* 4 (2013): 2322.

[35] Manz, Sebastian, et al. "Reversible optical switching of antiferromagnetism in TbMnO 3." *Nature Photonics* 10.10 (2016): 653.

[36] Wong, Anthony T., et al. "Strain driven anisotropic magnetoresistance in antiferromagnetic La0. 4Sr0. 6MnO3." *Applied Physics Letters* 105.5 (2014): 052401.

[37] Sapozhnik, A. A., et al. "Manipulation of antiferromagnetic domain distribution in Mn2Au by ultrahigh magnetic fields and by strain." *physica status solidi (RRL)–Rapid Research Letters*11.4 (2017): 1600438.

[38] Yan, Han, et al. "A piezoelectric, strain-controlled antiferromagnetic memory insensitive to magnetic fields." *Nature nanotechnology* 14.2 (2019): 131.

[39] Chen, Xianzhe, et al. "Electric field control of Néel spin–orbit torque in an antiferromagnet." *Nature materials* (2019): 1-5.

III. Magnetic Memory with Layered Magnetostrictive and Non-Magnetostrictive Materials

3.1. Introduction

As previously mentioned, layering different materials with desirable properties into composites is a promising method to create new materials with unique features.

This section presents the novel concept of layering highly magnetoelastic materials with low dissipation, high speed materials (low damping and low coercivity) to make composites that are beneficial for high frequency strain-controlled memory applications. Currently, there is a lack of understanding about the degree to which different materials in thicker magnetic stacks are exchange-coupled. This section addresses this shortcoming through both theory and experiment. The first part of this section presents the materials development and neutron scattering characterization of the chosen candidate material system, FeGa/NiFe. The second part describes a new micromagnetic modeling approach for approximating the interfacial exchange coupling effects that dominates the FeGa/NiFe's switching behavior.

FeGa was chosen because it is the second highest magnetostrictor known, and NiFe was chosen because of its low coercitvity, low damping, and frequent inclusion in magnetic radio-frequency applications.

3.2. Polarized Neutron Reflectometry as a Measurement Technique

Polarized neutron reflectometry (PNR) is an effective method of directly probing the thickness dependence of magnetization in thin-film stacks [1]. It is used in the following study on

FeGa/NiFe. Below, the basic physical principles of PNR are discussed, and the methods used to glean information from scattering data are presented.

In PNR, magnetically polarized neutrons are shot at shallow incident angles on the surface of a magnetic material. These neutrons scatter by either impacting the material's nuclei directly or by interacting with the material's magnetic lattice. Since the neutrons are polarized, their reflection from the target film is a function of the alignment between the film's magnetic orientation and the neutron beam's polarization direction. To examine depth profiles, the incident angle of the neutron beam is swept, causing the neutrons to travel a different distance in the target material before being reflected. The resulting reflectometry signal counts the number of reflected neutrons at a given scattering vector (denoted Q, in $1/\text{Å}$), which is defined as the difference between the incoming and reflected wave vectors (and so Q encodes the incident angle). The net reflected signal is a superposition of the scattering from both the nuclear and magnetic sources, and periodicity in this signal can be converted to either nuclear or magnetic real space characteristic lengths. This scattering process can be repeated using both spin "up" and spin "down" neutrons, resulting in an ability to resolve spin-dependent depth profiles. As an example,

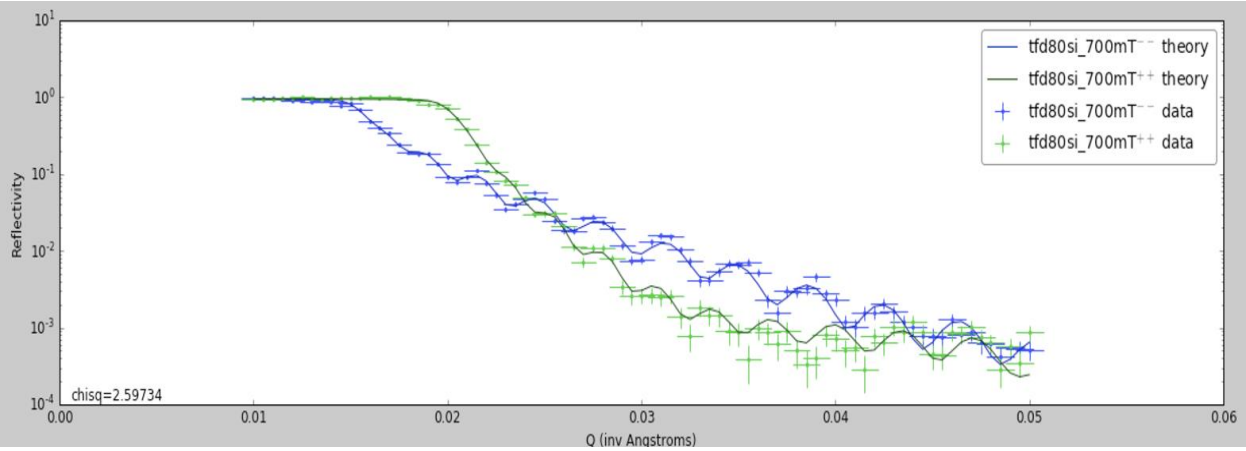

Figure 3.1 - The blue and green lines show a statistically significant fit to the spin up-up and spin down-down reflectometry signals. Parameters used in generating this fit include a real space depth-profile of the nuclear and magnetic scattering length densities.

Figure 3.1 shows an example of a PNR spectrum obtained from an 80 nm film of Terfenol-D grown on Si(001). The blue and green lines show a statistically significant fit to this data which yields first ever estimates of the nuclear and magnetic scattering lengths for unstrained Terfenol-D.

The fit to the data (solid lines in Figure 3.1) requires estimates of the real-space thickness-dependencies of the magnetic and nuclear scattering length densities, as well as the relative magnetization angle between the sample and the incident neutrons [2]. Since these parameters are unknown, they must be approximated. The nuclear scattering length density can be calculated by making a taking stoichiometry-based averages of known values for a material's constituent atoms. The relative magnetization angle is usually easy to estimate because most PNR measurements require that the sample sit inside of a bias field so as not to lose coherency of the incident neutrons. This applies for all cases besides those involving magnetic switching, where the angle must be estimated by other means. The magnetic scattering length density is a priori unknown, and must be estimated from micromagnetic calculations. For these reasons, the magnetic angle and depth profile are among the harder parameters to estimate.

For most single-phase or sufficiently thin layers, the magnetic angle and scattering density can be assumed to be constant across the thickness. In cases where films are thicker, there are large magnetic field gradients in the film, or the film contains multilayer stacks, fitting becomes difficult, and no standard micromagnetic calculation approach exists. Section 3.4 develops a new micromagnetic approach for solving this issue.

Once these parameters are estimated, the PNR spectrum is calculated by using the scattering length density profiles as space-dependent, discretized energy barriers for the incoming neutrons.

From here, the reflection coefficient of the entire material stack can be calculated using Schrodinger's equation for each discretized piece. Details can be found elsewhere [3].

3.3. Identifying Switched FeGa in FeGa/NiFe via Polarized Neutron Reflectometry

The idea to combine FeGa/NiFe was originally proposed by C. Rementer et al. in 2017 [4], with the motivation to create a magnetostrictive low-loss composite material for magnetic antenna applications. To validate the concept, C. Rementer first fabricated multilayer stacks of FeGa/NiFe and tested their resonance properties [4], finding that a repeated 7-bilayer structure resulted in 55% reduced linewidth, 88% reduced coercivity, and 67% maintenance of magnetostriction compared to single layer FeGa.

Based on these results, a candidate system was designed to study the thickness-dependence of these composite properties. In particular, three different single bilayer systems were fabricated. All three contained $Fe_{86}Ga_{14}$ with a 20 nm nominal thickness and a $Ni_{80}Fe_{20}$ top layer of varying thickness. The three NiFe thicknesses used were 7 nm, 20 nm, and 46 nm. All of the samples were sputter deposited on a 500-micron [100]-cut substrate of the single crystal piezoelectric $PbMg_{1/3}Nb_{2/3}O_3$-$PbTiO_3$ (PMN-PT).

The PNR measurements for each sample were taken at the Polarized Beam Reflectometer (PBR) beamline at the National Institute for Standards and Technology (NIST) in Gaithersberg, Maryland. Each sample was mounted in the beamline and saturated by a high magnetic field. Then the field was reduced to 10 Oe to leave a small magnetic bias. In this configuration, PNR spectra were obtained for both non-spin-flip (i.e. spin up-up and spin down-down) and spin-flip (i.e. spin up-down and down-up) polarizations.

The fits to the data implied coherent rotation for both the samples with 7 nm and 20 nm NiFe thickness, indicating that these thicknesses are sufficiently thin that they are fully exchange coupled. For this reason, their PNR spectra are essentially the same and the magnetic depth profiles are all uniform. The spectra for the 7nm sample is shown in Figure 3.2 for reference.

The spectra for the layer with 46 nm of NiFe, however, is different. The PNR fit to the data in this case is statistically improved by assuming a magnetic gradient in the NiFe layer which gets

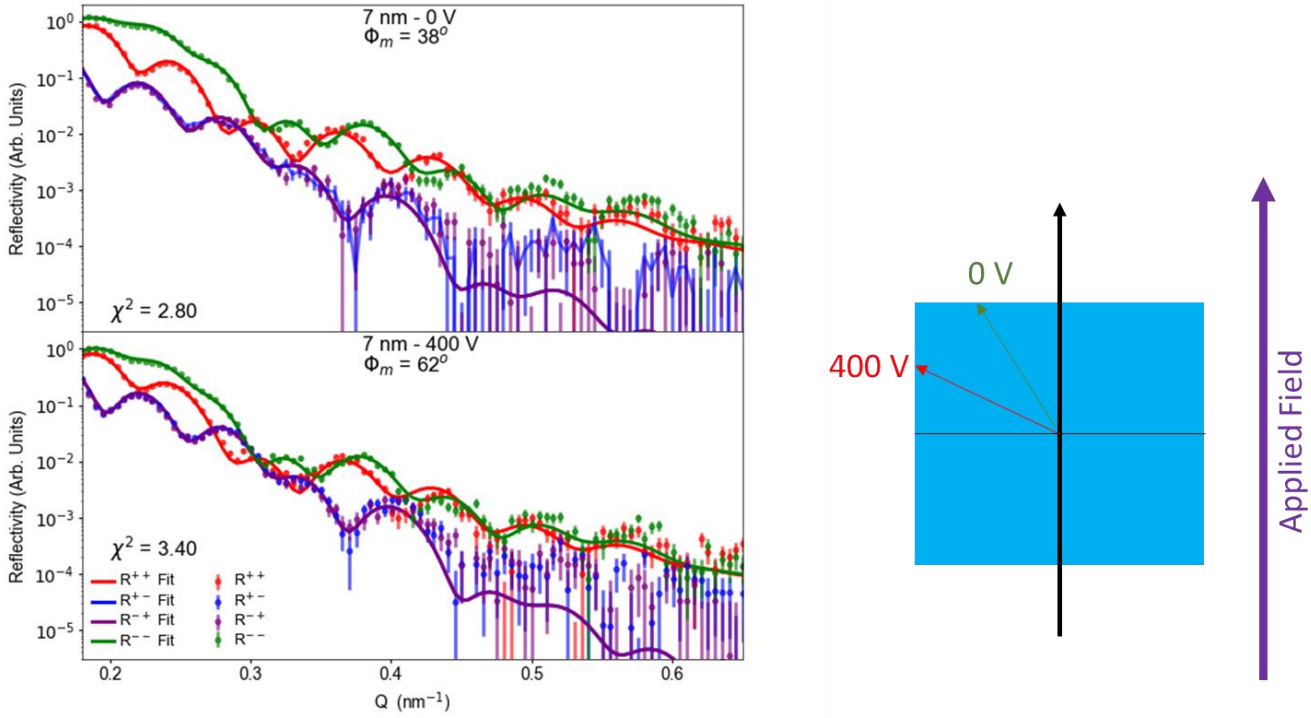

Figure 3.2 – (Top Left) The unstrained PNR spectra, i.e. with 0 V across the PMN-PT, is shown for the spin up-up (red), down-down (green), and spin flip (purple and blue) polarizations. Fit parameters indicate a 38˚ magnetization angle with the neutron polarization. (Bottom Left) The strained, 400 V PNR spectra, with fits indicating a 62˚ magnetization angle. (Right) A diagram shows the rotation with and without straining voltage.

larger after the PMN-PT-induced strain application. This would imply that strain serves to partially rotate the FeGa layer, and that the NiFe follows it, but that the top surface of the NiFe

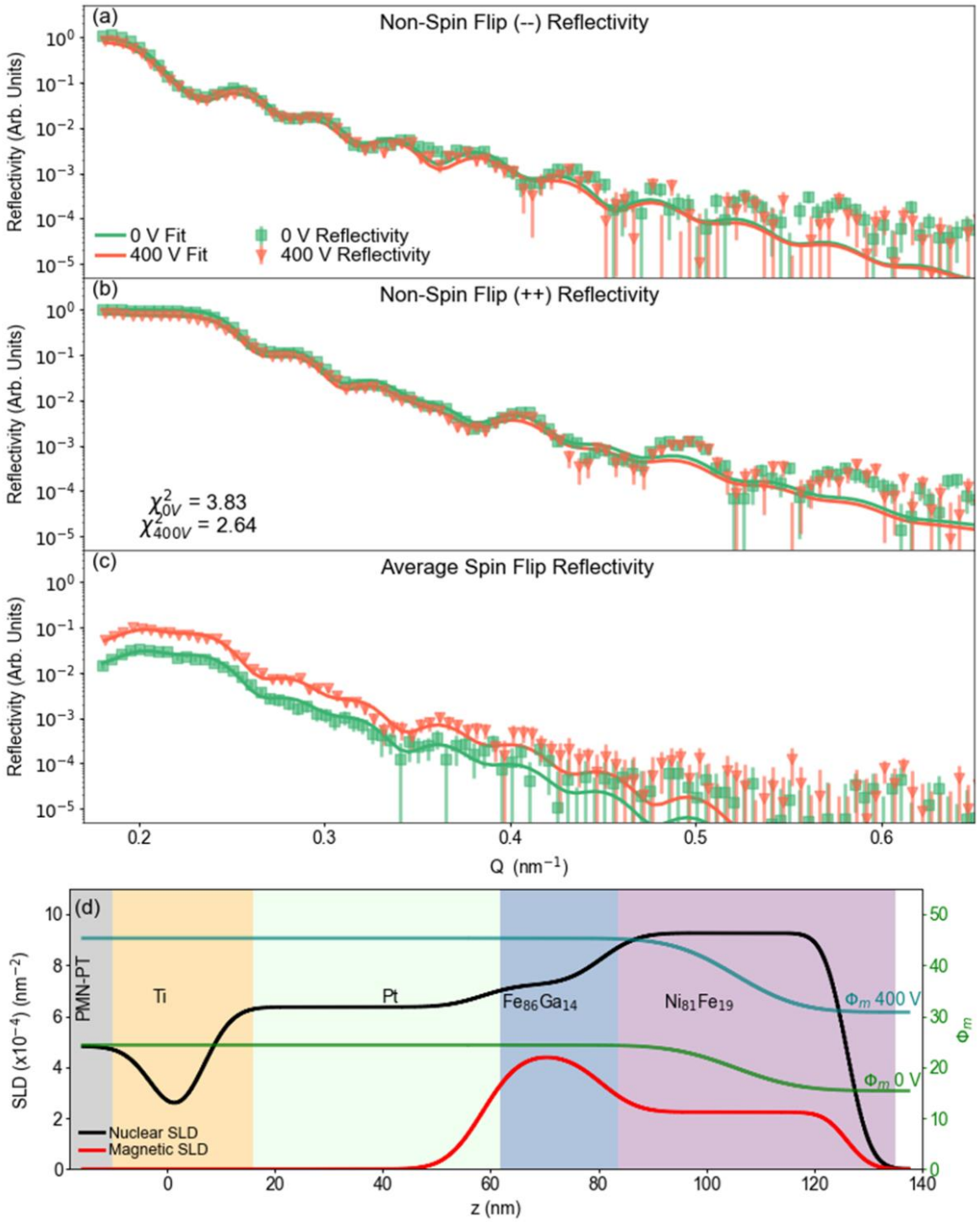

Figure 3.3 – (Top) The two top graphs show the non-spin-flip PNR fits, and the bottom graph shows the spin-flip fit. All indicate good agreement between fit and data. (Bottom) The depth profile of the nuclear and magnetic scattering length densities are shown (red and black), with the magnetization angles for the 0 V and 400V conditions in green and blue. Note the higher θ_m gradient at 400 V.

rotates less than the interface. Figure 3.3 shows a fit to PNR data that assumes this increased gradient in the magnetization of the NiFe layer (see the bottom of the figure).

To obtain the magnetic depth profile needed for the fit, the most sensitive parameter is the magnetic gradient, which has to be estimated by means other than PNR. As mentioned in sections 3.1 and 3.2, this was estimated using a novel micromagnetic approach.

3.3. Micromagnetic Estimation of Depth Profiles in Exchange-Coupled Multilayers

To estimate magnetic gradients in multilayer multiferroic composite, micromagnetic calculations can be used.

In this section, a new method is presented for applying these micromagnetic simulation methods to multilayer materials. The new method, based on FEA, accounts for differing magnetic properties between the layers, an additional interfacial exchange coupling term, and a decay of this interfacial exchange away from the interface. This newly developed model, which is implemented in COMSOL Multiphysics, is compared with a publicly available micromagnetics solver, MuMax 3 [5], which utilizes a finite difference time domain (FDTD) solver.

These two modeling approaches were applied to the three bilayer systems mentioned above, with 7, 20, and 46 nm of NiFe in the composite. For each case, the composite magnetization was initialized in-plane along the x-axis, and sufficient uniaxial anisotropy was applied to the $Fe_{86}Ga_{14}$ layer to rotate it 90 degrees to the y-axis. Then, the system was relaxed magnetically relax for 1 ns to reach a new equilibrium. Finally, the end-state in-plane components were plotted as a function of depth within the composite film.

The MuMax3 model, in particular, was intended to provide a lower-bound estimate of the magnetic gradient post-switching by 1) overestimating the strength of the interlayer exchange

coupling and 2) simulating the biaxial in-plane pinning effects of demagnetization in the large aspect ratio composite. To do this, a 500 x 500 x Z nm geometry was simulated, where Z represents the three possible total thicknesses variations mentioned above. The bottom 20 nm of each simulated magnetic volume was given the material properties of bulk amorphous $Fe_{86}Ga_{14}$ (M_s = 1300 emu/cc [6], A= 1.4 x 10^{-11} J/m^3 [6]), and the top Z-20 nm was given the properties of bulk $Ni_{80}Fe_{20}$ (M_s = 860 emu/cc [8], A= 1.3 x 10^{-11} J/m^3 [8]). This magnetic volume was then discretized into 2 x 2 x 1 nm cuboidal finite-difference-time-domain (FDTD) cells, whose size was chosen to be smaller than the exchange lengths of either $Ni_{80}Fe_{20}$ or $Fe_{86}Ga_{14}$. Since the as-grown films had an in-plane area of about 1 x 1 cm, the model included periodic boundary conditions at the x- and y-boundaries. Specifically, the periodic boundary conditions enforced 1) that **m** was equal at each opposing boundary, and 2) that 10 periodic repetitions, or images, of the geometry were added to the total geometry size when computing the demagnetization tensor. 10 repetitions of the geometry were sufficient for the simulation to reach a thin-film limit, meaning that the simulated behavior reflects that at the center of a large film. Since bulk material properties were used, no decrease of exchange coupling across (or away from) the $Ni_{80}Fe_{20}/Fe_{86}Ga_{14}$ interface was assumed. This means that the results of the MuMax3 model likely underestimate the through-the-thickness magnetic gradients which may be present in the real composite films.

Alternatively, the COMSOL model was designed to provide an upper-bound estimate of the gradient by 1) decreasing the interlayer exchange coupling by 1-3 orders of magnitude in accordance with reports on exchange-biased systems [9], and 2) implementing an interlayer exchange field that decays exponentially [10] away from the $Ni_{80}Fe_{20}/Fe_{86}Ga_{14}$ interface. Since the tuning of the interfacial exchange boundary conditions results in a strongly varying depth

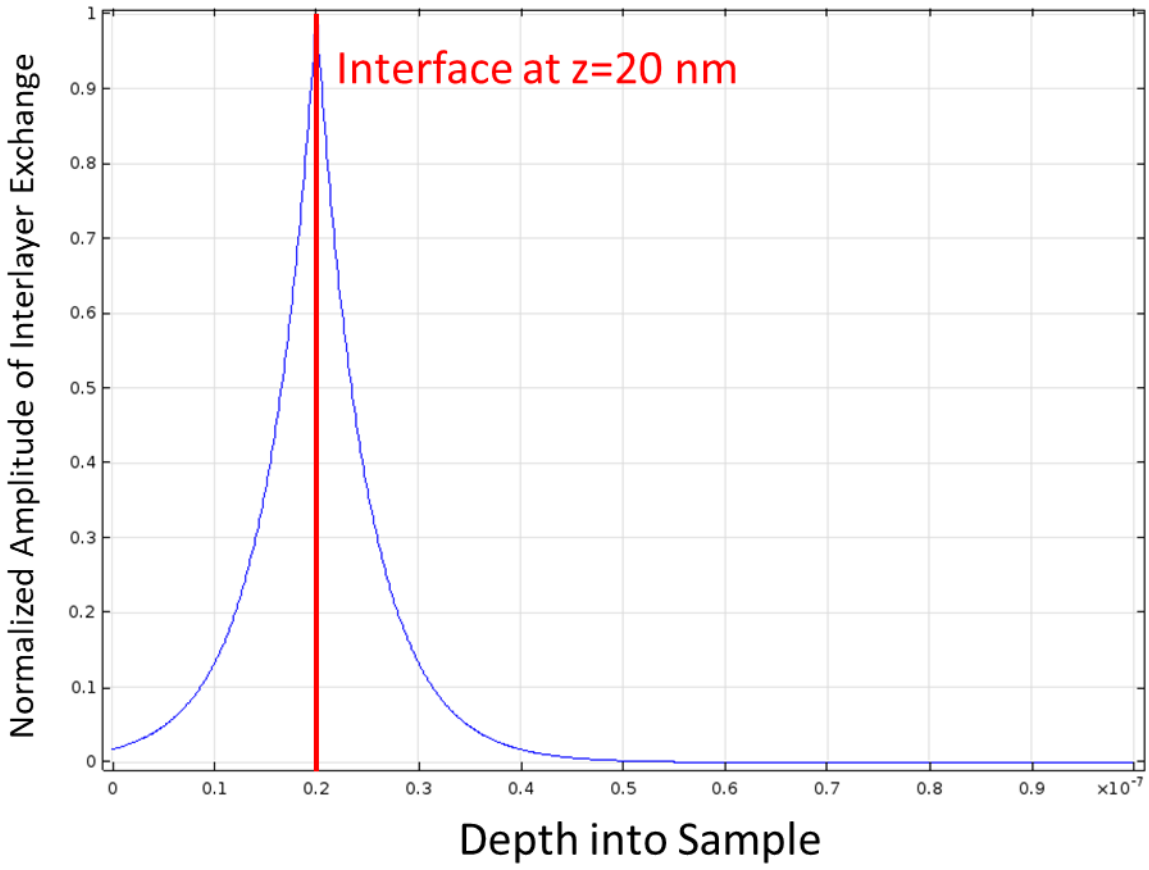

Figure 3.4 – The normalized interlayer exchange decay profile is plotted as a function of the sample depth, with the interface highlighted at z=20 nm.

profile of magnetic anisotropy, demagnetization effects were neglected. As a result, the system was modeled as a 6 x 6 x Z central slice of a large area film. This volume was discretized using a 3 x 3 x 1.2 nm cuboidal finite element mesh. As in the MuMax3 model, the bottom 20 nm were given the material properties of $Fe_{86}Ga_{14}$, and the top Z-20 nm were given the properties of $Ni_{80}Fe_{20}$. However, whereas the interlayer exchange effects were handled implicitly in MuMax3, the COMSOL model includes a specific interlayer exchange coupling energy defined by

$$E_{ex} = JR(\underline{m}^{FeGa} \cdot \underline{m}^{NiFe})$$

where J is the interlayer exchange coefficient in J/m^3, R is a unitless coefficient that proportionally reduces J when not every interfacial spin participates in coupling, and the

superscripts denote the material type. Since exchange coupling between other layered iron-containing magnetic alloys is known to be mediated through the iron moment, J was made equal to the bulk exchange constant for iron (3.97e7). Previous work in the field of exchange-biased multilayers has indicated that the value of R may range from $1/10$ to $1/1000$ depending on the material and interface condition [9]. Since R has never been measured in $Ni_{80}Fe_{20}/Fe_{86}Ga_{14}$ it was set to $1/20$ to yield relatively conservative estimates of magnetic gradient. To model the depth dependent decay of the interlayer exchange, the interlayer exchange field $H_{interlayer}$ was reduced by a function $E^d(z)$ that was created to exponentially decay from 1 at the interface, to 0, at a position 30 nm from the interface, as follows (see Figure 3.4 for more detail)

$$E^d(z) = e^{\frac{-1}{2*L_{ex}}(z-z_{int})}$$

where z the depth in the $Ni_{80}Fe_{20}/Fe_{86}Ga_{14}$ bilayer, z_{int} is the position of the interface (at z=20 nm), and L_{ex} is a magnetic decay length that was set to 2.5 nm. This decay function ensures that maximal coupling occurs at the interface and that the end-state equilibrium positions of the spins furthest from the interface depend only on each layer's internal exchange coupling.

Figure 3.5 shows the results obtained for both modeling methods following the procedure outlined here. Most importantly, as expected, the model predicts larger magnetic gradients in the thicker samples and, following the theory, MuMax3 tends to under-predict the gradients compared to COMSOL. The COMSOL model, however, tends to be very sensitive to the parameter R from Equation 3.1, meaning that exact quantitative agreement with experiment is not likely without additional experimental data to draw from. As a result, we recommend that

more experimental effort be focused towards identifying the interfacial exchange constants and decay behavior of multilayer systems.

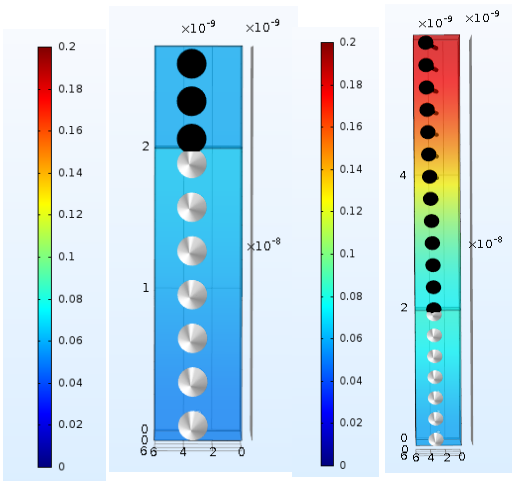

Δm (%)	7 nm	20 nm	40 nm
MuMax3	0.4%	1.2%	4.8%
COMSOL	0.37%	3.3%	14.9%

Figure 3.5 – (Left) The two diagrams indicate the end-state magnetic gradients for the samples with 7 nm (far left) and 20 nm (middle) thicknesses of NiFe. NiFe spins are pictured in black, and FeGa in white. The color gradients correspond with the magnitude of the y-component of the magnetization, with blue indicating 0 and red indicating 0.2 on a normalized scale to 1. (Right) A table shows the total magnetic gradient in the composite for each simulated case expressed as a percentage.

The results also show that, despite the interlayer exchange coupling dropping to zero at the top surface of the 40 nm NiFe film, the model still predicts reasonable rotation of the top surface (i.e. furthest from the interface). This indicates that the strong interfacial coupling first rotates the interfacial spins, and then the NiFe's own exchange coupling transfers this rotation all the way to the furthest spins at the top surface, more than 5 exchange lengths away. From this, is it possible to conclude that magnetic gradients in multilayers probably do not significantly contribute to magnetoresistive effects in multilayer magnetic memory. It is clear that even the largest magnetic gradients in the thickest magnetic films would be too small to reliably resolve via a memory-read process in a magnetoresistive memory. As a result, identifying magnetic gradients via magnetometry data (instead of PNR) is probably not promising either. However, the inability to remove long-distance even in designed systems means that the averaging of properties in

multilayers is probably mediated by the exchange energy, and can contribute significantly to the overall material behavior.

3.4. Conclusion

In this section, two advancements are reported.

First, a new micromagnetic modeling method for multilayers is reported. It is based on finite element simulation and incorporates interfacial exchange effects, as well as a decay of the interfacial coupling away from the multilayer interface. Due to the exponential nature of this decay, and unavailability of required material constants, this new model was seen to overpredict magnetic gradients. The new model was compared to MuMax3, a publicly available solver, which tends to underestimate magnetics gradients. Based on these results, further materials research is recommended regarding interfacial coupling coefficients and their decay functions.

This section also confirms that layering magnetoelastic and non-magnetoelastic materials into composites does result in an averaging of their properties as long as the composite thicknesses stay around three exchange lengths. Both micromagnetic simulation and PNR data reported here indicate that magnetic decoupling of the layers for larger composite thicknesses.

Despite the positive results presented here, the potential for drastic material improvements via multilayering is limited (around 50%). For this reason, antiferromagnets are recommended for a much larger improvement. Further reasoning is provided in the next section.

3.5. Chapter References

[1] Majkrzak, C. F. "Polarized neutron reflectometry." *Physica B: Condensed Matter* 173.1-2 (1991): 75-88.

[2] Jamer, Michelle E., et al. "Long-Range Electric Field Control of Permalloy Layers in Strain-Coupled Composite Multiferroics." *Physical Review Applied* 10.4 (2018): 044045.

[3] Maranville, Brian B. "Interactive, Web-Based Calculator of Neutron and X-ray Reflectivity." *J. Res. Nat. Inst. Stand. Technol* 122 (2017): 1.

[4] Rementer, Colin R., et al. "Tuning static and dynamic properties of FeGa/NiFe heterostructures." *Applied Physics Letters* 110.24 (2017): 242403.

[5] Vansteenkiste, Arne, and Ben Van de Wiele. "MuMax: A new high-performance micromagnetic simulation tool." *Journal of Magnetism and Magnetic Materials* 323.21 (2011): 2585-2591.

[6] Chavez, Andres C., Anthony Barra, and Gregory P. Carman. "Voltage control of magnetic monopoles in artificial spin ice." *Journal of Physics D: Applied Physics* 51.23 (2018): 234001.

[7] O'handley, Robert C. *Modern magnetic materials: principles and applications*. Wiley, 2000.

[8] Kinane, C. J., et al. "Soft x-ray resonant magnetic scattering from an imprinted magnetic domain pattern." *Applied physics letters* 89.9 (2006): 092507.

[9] Kiwi, Miguel. "Exchange bias theory." *Journal of Magnetism and Magnetic materials* 234.3 (2001): 584-595.

[10] Chumak, Andrii V., et al. "Spin-wave propagation in a microstructured magnonic crystal." *Applied Physics Letters*95.26 (2009): 262508.

IV. Magnetic Memory with Antiferromagnets: A Theoretical Perspective

4.1. Introduction

While the previous chapter highlighted the possibility for magnetic multilayers to improve the high frequency loss characteristics of memory by 50%, much larger improvements are needed. THz switching speeds are attractive, especially if these high speeds can come with an energy savings. The energy savings of multiferroics at the nanoscale have already been proven, with a predicted ~10 aJ/state switch [1-2], but if these multiferroics use ferromagnetic materials, their frequency response is limited by ferromagnetic resonance (usually ~1-10 GHz). Consequently, antiferromagnets are attractive alternatives, because they exhibit resonances 2-3 orders of magnitude higher (~1 THz) [3-4], however, they are difficult to manipulate with external fields because the applied field needs to overcome the exchange anisotropy and induce a spin flop transition (which usually occurs for >1 Tesla). This section proposes solving the 1 Tesla control problem by leveraging magnetoelastic coupling found in antiferromagnets like NiO [5-6], [37-40] or FeMn [7]. In particular, the uniaxial nature of the strain anisotropy enables rotation of the antiferromagnet phase without overcoming the antiferromagnetic exchange, and this lowers the required switching anisotropy by a factor of 10-100 times. To further analyze dynamics in such systems, we present a numerical framework which solves the 10 coupled partial differential equations that govern spatiotemporal magnetoelastic response in antiferromagnet-piezoelectric composites, and demonstrate energy efficient, ultra-fast switching. This strain-mediated voltage control of magnetism offers a new pathway to drive dynamic processes, on-chip, within the THz bandgap between radio and optical frequencies for the first time. This advancement may enable a new generation of strain-coupled antiferromagnetic sensors, spin wave devices, and systems with

tunable exchange-biasing. Our findings also provide a clear direction for future research efforts to find magnetoelastic antiferromagnets with low intrinsic anisotropy.

Previous modeling efforts focused on predicting magnetoelastic dynamics in ferromagnets [8-10]. These models accounted for spatial non-uniformities in both strain and magnetization, thereby providing predictions that agreed with experimental data more closely than single-spin Stoner-Wohlfarth models or micromagnetic Landau-Lifshitz-Gilbert (LLG) models that assume uniform strain (i.e. mechanically decoupled models). Magnetoelastic models have been used to analyze voltage-controlled 180˚ switching in magnetic nanoelements with perpendicular magnetic anisotropy [11], in-plane magnetic switching driven by selective piezostraining using patterned electrodes [12-13], and 360˚ control of domain wall rotation in nickel ring structures [14] to name a few [15]. However, dynamic magnetoelastic models of antiferromagnets have received little attention, and most antiferromagnetic models focus only on the micromagnetic behavior rather than mechanical coupling effects [16-17]. In particular, micromagnetic modeling has been used to predict the behavior of exchange-biased multilayers, specifically using finite elements [18] and the Monte Carlo method [19-20]. In experimental work, only magnetoelectricity in single phase materials [21-23] and carrier-induced spin reorientation [24-25] have previously been used for antiferromagnetic domain control. This section provides continuum-level numerical modeling illustrates that magnetoelasticity can provide a high speed, low power alternative control method for microscale antiferromagnets.

4.2 Micromagnetic Model Development

In this section, we provide the equations governing the spatiotemporal evolution of an antiferromagnetic material in response to voltage-induced strain. This formalism assumes that any antiferromagnetic phase can be deconstructed into two constituent ferromagnetic sublattices which

are antiferromagnetically exchange coupled and oppositely oriented in the absence of external stimuli. Each of these sublattices is further assumed to be locally magnetically saturated throughout the entire volume. The sublattice magnetic moments are described by the vector field components $m_i^{(s)}(t)$, where i = {1,2,3} indicates the direction in a Cartesian coordinate system, and s = {1, 2} indicates the sublattice. The model also assumes magneto- and electrostatics, infinitesimal strains, and neglects thermal influences.

Under these conditions, the dynamics of each magnetic sublattice follow the LLG equation [26],

$$\frac{\partial \underline{m}^{(s)}}{\partial t} = -\gamma \underline{m}^{(s)} \times \underline{H}_{eff} - \alpha \underline{m}^{(s)} \times \frac{\partial \underline{m}^{(s)}}{dt} \tag{1}$$

Where γ is the gyromagnetic ratio, $\underline{H}_{eff}$ is the effective magnetic field, $\underline{m}^{(l)}$ is the sublattice magnetization direction, and α is the Gilbert damping parameter. $\underline{H}_{eff}$ is the driving term of the magnetic dynamics in Equation 1. It can vary in space and time, and is determined by taking the functional derivative of the total free energy density E_{total}

$$\underline{H}_{eff}^{(s)} = \frac{-1}{\mu_0 M_s} \frac{\partial E_{total}}{\partial \underline{m}^{(s)}} \tag{2}$$

where μ_0 is the vacuum permeability and M_s is the saturation magnetization. Equation 2 indicates that $\underline{H}_{eff}$ will contain a term for each magnetic anisotropy energy that contributes to E_{total}. In antiferromagnets with negligible magnetocrystalline anisotropy the relevant energy densities are

$$E_{total} = E_{ex}^{(1)} + E_{ex}^{(2)} + E_{AFM}^{(1-2)} + E_{me}^{(1)} + E_{me}^{(2)} \tag{3}$$

where E_{ex}, E_{AFM}, and E_{me} denote the intralattice ferromagnetic exchange, the interlattice antiferromagnetic exchange, and magnetoelastic energy densities, respectively. This formulation of the energy densities assumes that all anisotropies besides those listed in Equation 3 are low relative to the strain-induced anisotropy. This assumption is reasonable as many magnetoelastic ferromagnets (Ni or FeGa), ferrimagnets (TbDyFe), and antiferromagnets (FeMn, MnNi, IrMn) [41-43] have low magnetocrystalline (MCA) or shape anisotropies relative to the strength of strain coupling. Including any of these smaller additional anisotropies like MCA or shape anisotropy would result in the formation of preferred axes of magnetic alignment (i.e. stable states), and modify the switching dynamics by creating energy wells which the strain-excitation must overcome. Since these changes may be complex, the model presented here addresses only amorphous antiferromagnets that are isotropic in-plane with stable states dictated by the exchange and magnetoelastic energies in Equation 3. The form of E_{ex} used here is common in the literature $E_{ex}^{(s)} = A\nabla^2 \underline{m}^{(s)}$ [8][41], where A is the exchange stiffness. The interlattice antiferromagnetic exchange is defined by an Ising-like term $E_{AFM}^{(1-2)} = -J\,\underline{m}^{(1)} \cdot \underline{m}^{(2)}$, where J is the antiferromagnetic exchange coupling coefficient. In most antiferromagnets J is sufficiently large that $-\underline{m}^{(1)} \approx \underline{m}^{(2)}$ [27], which cancels the dipolar fields and leads to zero demagnetization energy. The two remaining terms, $E_{me}^{(1)}$ and $E_{me}^{(2)}$, are functions of both strain and $\underline{m}^{(s)}$

$$E_{me}^{(s)} = \frac{1}{2}\left(\sum_i B_1 \varepsilon_{ii}^{total} (m_i^{(s)} m_i^{(s)} - \frac{1}{3}) + \sum_{i \neq j} B_2 \varepsilon_{ij}^{total} m_i^{(s)} m_j^{(s)} \right) \tag{4}$$

where B_1 and B_2 are the first and second order magnetoelastic coefficients.

Next, we present the effective fields used in the model, discuss the magnetomechanical coupling terms, and examine their connection to elastodynamic behavior. The two intralattice exchange fields are represented using the conventional ferromagnetic exchange term $H_{ex}^{(l)} = 2A(\mu_0 M_s)^{-1}\nabla^2 \underline{m}^{(l)}$ [28]. In contrast, the antiferromagnetic exchange field $H_{AFM}^{(s)}$ contains terms which allow the magnetization of one sublattice to influence the other. The ith component of these fields in each sublattice, respectively, are

$$\left[H_{AFM}^{(1)}\right]_i = -\frac{Jm_i^{(2)}}{\mu_0 M_s^{(1)}} \quad \text{and} \quad \left[H_{AFM}^{(2)}\right]_i = -\frac{Jm_i^{(1)}}{\mu_0 M_s^{(2)}} \tag{5}$$

To simultaneously solve the coupled magnetoelastic dynamics, two additional coupling terms are needed. One of these terms, $H_{me}^{(l)}$, is an effective field that changes the sublattice magnetic state based on the total strain $\underline{\underline{\varepsilon}}^{total}$. The ith component of $H_{me}^{(l)}$ is

$$\left[H_{me}^{(s)}\right]_i = -\frac{1}{\mu_0 M_s^{(s)}}\left(B_1 \varepsilon_{ii}^{total} m_i^{(s)} + \sum_{j\neq i} B_2 \varepsilon_{ij}^{total} m_j^{(s)}\right) \tag{6}$$

where summation occurs only in the second term. This paper focuses on systems with isotropic magnetostriction, a condition which requires $\lambda_{100} = \lambda_{111} = \lambda_{110}$ and $B_1 = B_2$. Furthermore, the magnetostrictive coupling was assumed to affect each sublattice equally. This required 1) halving the magnitude of $\left[H_{me}^{(s)}\right]_i$ in equation 6 in comparison to the form for ferromagnets, and 2) defining $B_1^{Fe} = B_1^{Mn}$ and $B_2^{Fe} = B_2^{Mn}$. To maintain the self-consistency of the model, this reduction by half was also included in the magnetoelastic strain coupling term, $\underline{\underline{\varepsilon}}^{ME}$, which defines the strain caused by magnetic reorientation

$$\varepsilon_{ij}^{ME} = \frac{1}{2}\lambda_s \left(\frac{3}{2}\left[m_i^{(1)} m_j^{(1)} - \frac{1}{3} \right] + \frac{3}{2}\left[m_i^{(2)} m_j^{(2)} - \frac{1}{3} \right] \right) \tag{7}$$

where λ_s is the saturation magnetostriction. In the limiting case of equation 7, when an antiferromagnet is uniformly magnetized, $\left| m_i^{(s)} m_j^{(s)} \right| \to 1$ and $\underline{\underline{\varepsilon}}^{ME} \to \lambda_s$ along the axis of magnetization. This implies that saturation magnetostriction occurs when the two sublattices are coaxially aligned. Analogous behavior is observed in ferromagnets in the limit of magnetic saturation [26].

Equations 6-7 ensure that the mechanical and magnetic dynamics are coupled and can be solved simultaneously. However, calculation of $\underline{\underline{\varepsilon}}^{total}$ in equation 6 requires that the system's elastodynamics be considered. The governing equation of linear elastodynamics is

$$\rho \frac{\partial^2 \underline{u}}{\partial t^2} - \nabla \cdot \underline{\underline{\sigma}} = 0 \tag{8}$$

$$\underline{\underline{\sigma}} = \underline{\underline{\underline{\underline{C}}}} : \underline{\underline{\varepsilon}}^{mech} \tag{9}$$

where ρ is the material density, $\underline{u}$ is the displacement, $\underline{\underline{\sigma}}$ is the elastic stress, $\underline{\underline{\underline{\underline{C}}}}$ is the stiffness, and $\underline{\underline{\varepsilon}}^{mech}$ is the elastic strain. The driving term in equation 9 is the mechanical strain $\underline{\underline{\varepsilon}}^{mech}$, which is the difference between the total strain $\underline{\underline{\varepsilon}}^{total}$ and the magnetic strain $\underline{\underline{\varepsilon}}^{ME}$. In this paper, we also consider cases where the antiferromagnet is externally strained by a piezoelectric material, in which case $\underline{\underline{\varepsilon}}^{mech}$ becomes

$$\underline{\underline{\varepsilon}}^{mech} = \underline{\underline{\varepsilon}}^{total} - \underline{\underline{\varepsilon}}^{piezo} - \underline{\underline{\varepsilon}}^{ME} \tag{10}$$

where $\underline{\underline{\varepsilon}}^{piezo}$ is the piezostrain. The strains in equation 10 are directly related to the physical displacements through $\underline{\underline{\varepsilon}}^{total} = \frac{1}{2}\left(\nabla \underline{u} + (\nabla \underline{u})^T\right)$.

Equations 2-7 and 9-10 were inserted into equations 1 and 8, resulting in nine coupled partial differential equations that govern antiferromagnetic magnetoelastic dynamics. In the case where piezoelectricity was included, one more differential equation was added to calculate the electric field distribution inside the piezoelectric layer. The coupled PDEs were solved simultaneously using a weighted residuals method within a finite element framework. The finite element solver used implicit time stepping ($t_{step}^{(\max)} = 0.5$ ps) and a backward differentiation formula. In the antiferromagnetic volume, a cuboidal finite element mesh was used, with a maximum element size of 2.5 x 2.5 x 0.57 nm^3. This element size was chosen to capture any magnetic non-uniformities within the antiferromagnet's constituent ferromagnetic sublattices on the order of the exchange length, $L_{ex} = (2A_{ex})/(\mu_0 M_s{}^2)^{1/2} \approx 3.51$ nm, while simultaneously capturing any strain variations due to effects like shear lag.

The model developed above was used to study the two cases shown in Figures 4.1(a)-(b). In the first case (Figure 4.1(a)), an antiferromagnetic disk with an 80 nm radius and 4 nm thickness was modeled with traction free boundary conditions ($\underline{t} = \underline{\underline{\sigma}} \cdot \underline{n} = 0$) imposed at every surface. First, the disk's antiferromagnetic state was initialized out-of-plane (along e_3) and relaxed for 50 ps. Then, at t=0, a uniform strain field was applied everywhere in the volume, with 1000 με of tension along e_2 and 400 με of compression along e_1. The average sublattice magnetic response was then

recorded every 0.5 ps. Fourier analysis of the sublattice response to the broadband excitation allowed for identification of the antiferromagnetic resonance frequency.

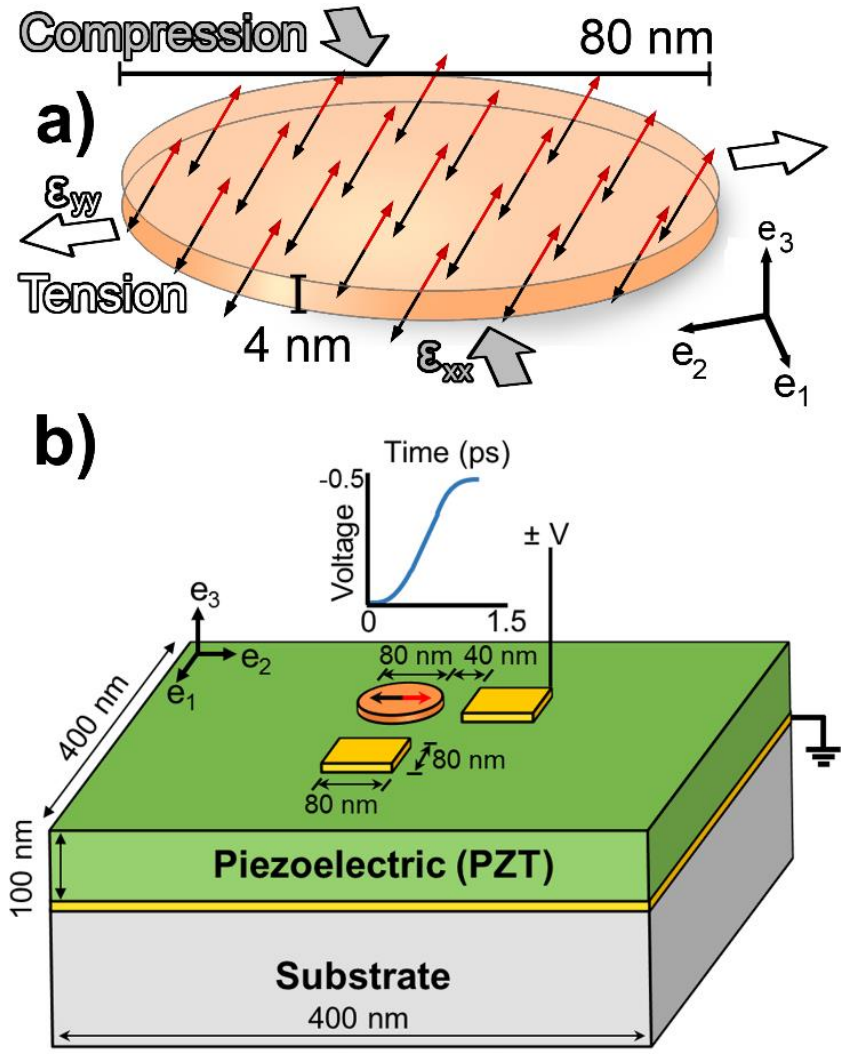

Figure 4.1 -The geometries used in the finite element calculation are shown. (a) The geometry for the first model is a disk of diameter 80 nm and thickness 4 nm. The antiferromagnetic state is initially aligned out-of-plane and, after magnetically relaxing for 50 ps, remains unmoved. Then, at t=0, the displacement field inside the disk is precisely controlled to yield a uniform biaxial strain of 1400 με, with tension along e_2 and compression along e_1. (b) The geometry for the magnetomechanical model of the antiferromagnetic-piezoelectric composite is shown. In this structure, voltages can be applied at either of the two yellow electrodes (with electrical ground on the bottom planar electrode) to generate in-plane strains that can switch the antiferromagnetic state 90˚. The choice of electrode dictates the eventual in-plane direction of the switched antiferromagnet.

In the second model (Figure 4.1(b)), an antiferromagnetic disk was attached to a thin piezoelectric film which, in turn, was attached to a thick substrate. The 400 x 400 x 100 nm^3 piezoelectric film was modeled with a mechanically clamped bottom surface ($\underline{u} = 0$) and fixed in-plane boundaries ($\underline{u} \cdot n = 0$) to replicate the presence of the thick substrate and infinite extension of the film in the e_1-e_2 plane. The top surface of the composite was maintained traction free. As in the previous model, the disk's antiferromagnetic state was first initialized out-of-plane and relaxed for 50 ps. After relaxation, electrical ground (V = 0) was applied to the piezoelectric layer's bottom surface, while a voltage excitation, applied at either of the two 40 x 40 nm surface electrodes, was ramped from 0 to -0.5 V over 1.5 ps (see Figure 4.1(b) inset). The resulting piezostrain (see Figure 4.2 for

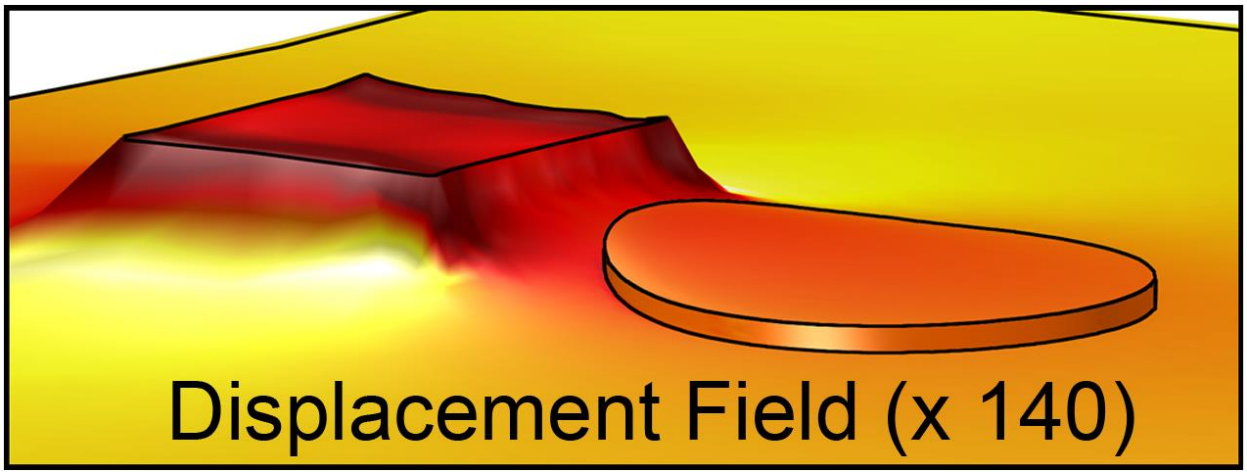

Figure 4.2 - The FEA calculated displacement profile of the antiferromagnetic bit (ellipse) and piezoelectric substrate during application of 0.8 MV/m of electric field (at the square electrode on the left).

the steady-state displacement profile) drove magnetic precession in the disk, which was recorded every 0.5 ps. As with the previous model, these boundary conditions were chosen because they lead to high but realistic strains, like those required for switching in other magnetoelastic materials.

The material properties used for both studies were as follows (bulk values were used where values for microscale geometries were not available, as they are known to be similar [34-36]). Since the

material properties of magnetostrictive antiferromagnets are not well-studied, the following constants were obtained from the available literature, using known constants for the ferromagnetic sublattices where relevant: $A_{ex\,(Fe)} \approx A_{ex\,(Mn)} = 2.48 \times 10^{-12}$ J/m [29], $M_{s\,(Fe)} \approx M_{s\,(Mn)} = 5.66 \times 10^5$ A/m, $\lambda_s \approx 750$ με [7], [30], Young's modulus $E = 77$ GPa [31], $\rho = 7700$ kg/m^3, and Poisson's ratio $\upsilon = 0.3$. A Gilbert damping parameter of $\alpha = 0.02$ was assigned to each ferromagnetic sublattice since this value is in the typical range for magnetoelastic ferromagnets [1, 43-44]. With these constants, the material modeled has a likeness to $Fe_{50}Mn_{50}$, whose antiferromagnetic exchange coupling coefficient, J_{AFM}, is currently unmeasured. Consequently, the value of the ferromagnetic exchange coefficient of bulk single crystal Fe, $J = 3.97 \times 10^6$ J/m^3, was used. In addition, a parametric sweep of α between 0.8 and 0.02 was used to confirm that value used for the Gilbert damping parameter did not significantly influence the threshold strain required for switching for realistic values of α (< 0.1). However, non-physical, high α values (> 0.7) produced a strongly overdamped response that changed the antiferromagnet's mechanical impedence and reduced strain transfer across the composite interface. For this reason, low α was used. With the material parameters used above, the magnetic and magnetostrictive predictions of the model cannot be quantitatively accurate for a particular material, but are intended to represent correct trends in the material behavior and exemplify proper modeling methods. The piezoelectric layer's properties were those of transversely isotropic $Pb[Zr_xTi_{1-x}]O_3$ (PZT). These were $d_{13} = -6.62$ C/m^2, $d_{33} = 23.24$ C/m^2, $\rho = 7500$ kg/m^3, $E_1 = 127$ GPa, $E_2 = 82$ GPa, $G_{13} = 22.9$ GPa, $\varepsilon_{11} = \varepsilon_{22} = 3130$, and $\varepsilon_{33} = 3400$.

4.3. Results and Discussion

Figure 4.3(a) shows the results for the model geometry illustrated in Figure 4.1(a) after uniform strain was applied at t=0 ps. The components of the Fe sublattice magnetization, $m_1^{(Fe)}$ (dashed line), $m_2^{(Fe)}$ (solid line), $m_3^{(Fe)}$ (dot-dashed line), and the magnitude of the net moment, $|L| = |\underline{m^{(Fe)}} + \underline{m^{(Mn)}}|$ (dotted line), were plotted as a function of time. The $m_2^{(Fe)}$ trace indicates that the sublattice realigned to the e_2-axis within 3.25 ps, and then oscillated about this new orientation for ~10 ps before stabilizing. During the same time, $m_1^{(Fe)}$ and $m_3^{(Fe)}$ exhibited precessional decay at a lower frequency, proportional to the applied switching anisotropy. The degree of magnetic sublattice misalignment, $|L|$, grew initially during the switching event in a manner proportional to $\frac{d\underline{m}}{dt}$. This sublattice misalignment was caused by the uniaxial nature of the switching anisotropy, which applied oppositely-pointing torques to the two sublattices. In turn, this drove the

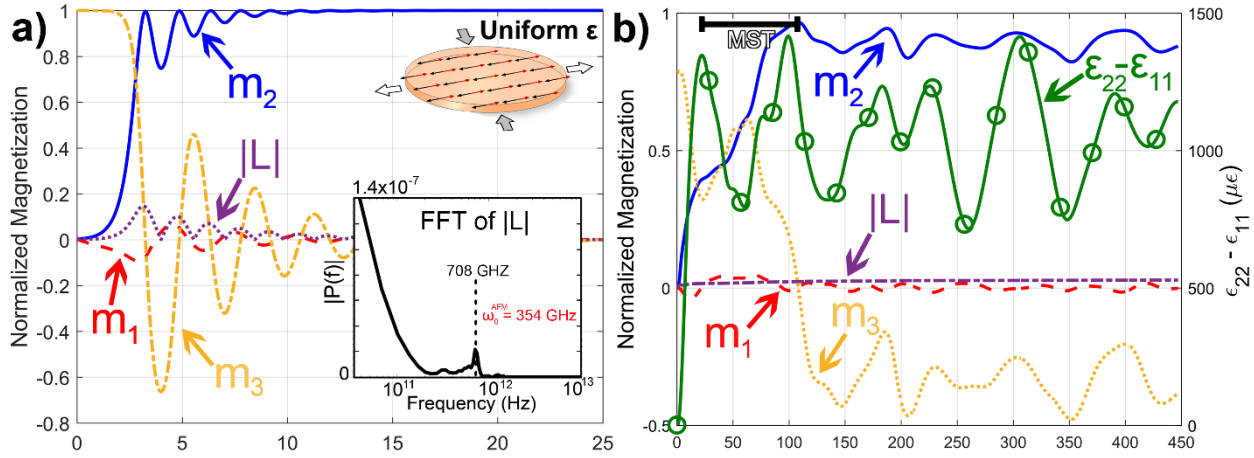

Figure 4.3 - The volume-averaged magnetization of the Fe sublattice is plotted in time domain for both models. (a) When uniform biaxial strain is instantaneously applied at t=0, the axis of antiferromagnetic alignment resonantly switches within 3.25 ps, and settles about 12 ps later. The peak in the FFT of $|L|$ at 708 GHz corresponds with an antiferromagnetic resonance at half that value, i.e. at 354 GHz (b) When voltage is applied at t=0, antiferromagnetic switching occurs after about 100 ps. The switching process proceeds so far below resonance as to be quasistatic. The observed continuation of motion in m_2 is owed to the continuing oscillation in biaxial strain (green line), which occurs because the exciting acoustic wave internally reflects within the antiferromagnetic disk.

sublattices to precess to the new easy axis with opposite chirality, thereby generating a net moment that reached a maximum of 7.3% of M_s at t=3.25 ps (as $m_2^{(Fe)}$ saturated). In the subsequent 10 ps, L oscillated with a periodicity that matched the ringing period observed in $m_2^{(Fe)}$. The similarity between these periods suggests that the system relaxed through the pendulum-like motion of the two sublattices about one another at antiferromagnetic resonance. The Fast Fourier Transform (FFT) of $|L|$ is known to exhibit a peak at twice the antiferromagnetic resonance (AFMR). For the modeled system, this peak occurred at 0.708 THz (shown in the inset of Figure 4.3(a)), which corresponds with a model-predicted AFMR of 0.354 THz. This simulated resonance is within about 28% of that predicted by theory [42]. The FFT also exhibited some high amplitude, low frequency content, which is attributed to the amplitude decay envelope of $|L|$.

Figure 4.3(b) shows the results for the voltage-actuated piezoelectric/antiferromagnetic composite model (from Figure 4.1(b)). In this model, voltage was applied at t=0 ps at the left-most electrode in Figure 4.1. The values of $\underline{m}^{(\mathrm{Fe})}$ and $|L|$ were plotted together with the volume-averaged biaxial strain state $(\varepsilon_{22} - \varepsilon_{11})$ in the antiferromagnetic disk (on the right ordinate axis). Prior to the application of voltage (i.e., during the magnetic relaxation period, t < 0), magnetoelastic torqueing occurred due to mechanical shear lag effects at the disk edges [8], producing a non-uniform initial sublattice magnetization state with the volume-averaged components $\underline{m}^{(\mathrm{Fe})}$ = (0, 0, 0.78). Then voltage was applied at t=0, and it took 18.5 ps for the voltage-induced strain wave to propagate from the electrode to the edge of the antiferromagnetic disk, as indicated by the first peak in the $\varepsilon_{22} - \varepsilon_{11}$ plot. It took an additional 84 ps (labeled MST in Figure 4.3(b)) for the strain to propagate across the disk and cause 90˚ rotation of $\underline{m}^{(\mathrm{Fe})}$. This is seen by the peak of $m_2^{(Fe)}$ concurring with

the second peak in $\varepsilon_{22} - \varepsilon_{11}$. Throughout the MST, $m_3^{(Fe)}$ decayed towards zero, as expected, but did not settle completely due to the system's continued strain oscillations. In contrast, $m_1^{(Fe)}$ remained relatively constant near zero during switching, since the switching occurred primarily in the e_2-e_3 plane. With regards to $|L|$, it remained stable around < 2% and, in contrast with the uniform strain model, it did not vary with $\frac{d\underline{m}}{dt}$ in the early part of the MST. These small values of $|L|$ indicate that the voltage-induced switching proceeded below the antiferromagnetic resonance (i.e., near adiabatically [32]), a phenomena also not observed in the uniformly strained model (Figure 4.3(a)). Subsequent Fourier analysis of $|L|$ indicated broadband low frequency response, which confirms the quasistatic nature of the switching. Further simulations showed that subsequent

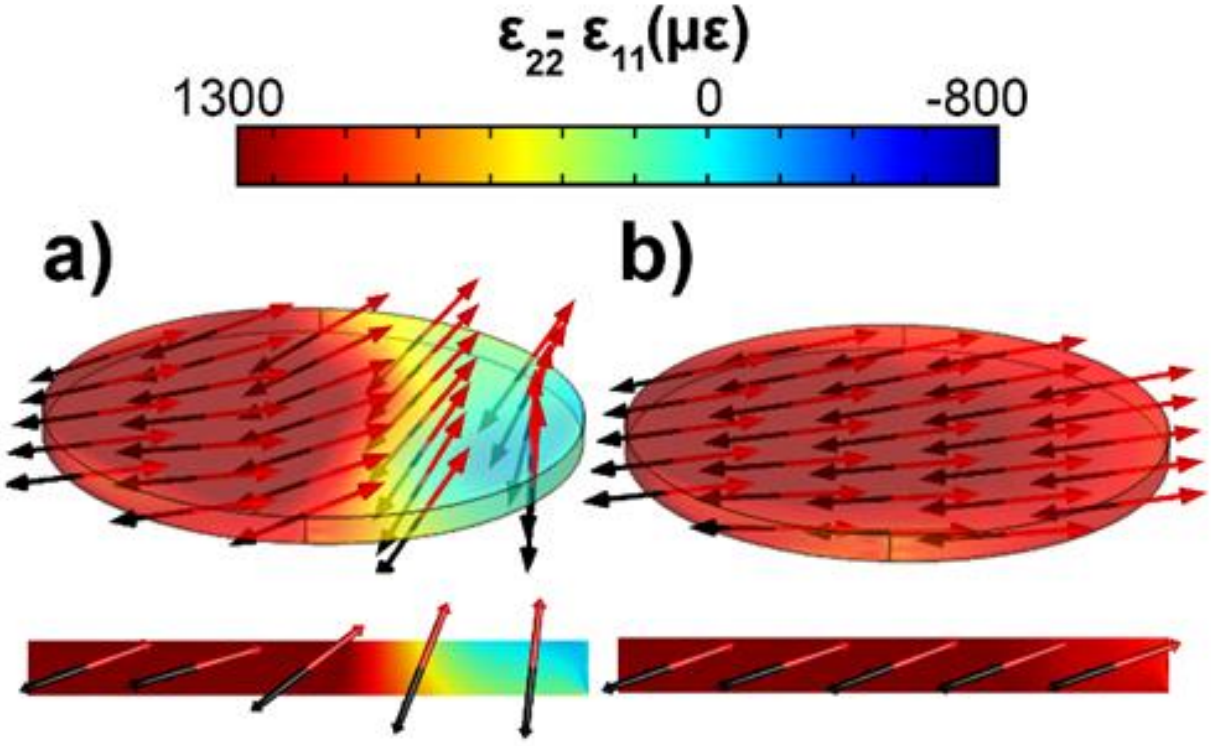

Figure 4.4 - The FEA calculated displacement profile of the antiferromagnetic bit (ellipse) and piezoelectric substrate during application of 0.8 MV/m of electric field (at the square electrode on the left).

voltage application to the other top surface electrode in Figure 4.1(b) resulted in 90˚ in-plane switching from e_2 to e_1 with the same frequency response observed during out-of-plane to in-plane switching.

The comparatively slow switching speed of the antiferromagnetic-piezoelectric composite is explained by observing the spin and strain states at two different times, as shown in Figure 4.4. In Figures 4.4(a)-(b), for t=71.5 ps and t=102.5 ps respectively, 3-dimensional plots of strain and magnetization are provided from a perspective view (top) and a cross-sectional view (bottom). In Figure 4.4(a), the strain wave during the MST, indicated by color gradient from red to blue (high strain is red, low strain is blue), had reached the middle the disk. At the same time, the magnetic moments in the strained portion of the disk had rotated in-plane, as shown by red ($\underline{m}^{(\mathrm{Fe})}$) and black ($\underline{m}^{(\mathrm{Mn})}$) arrows, whereas the moments in the unstrained portion of the disk did not move. By the end of the MST, Figure 4.4(b) shows that the strain had propagated through the entire disk and, correspondingly, the magnetization had rotated uniformly in-plane. Therefore, it is evident that the speed of antiferromagnetic reorientation is dictated by the speed at which strain can propagate through the disk.

While the uniform strain model suggests that near THz switching in an antiferromagnet is possible, the results from the composite model indicate that, for realistic strain-actuated structures, consideration must be given to the method of mechanical actuation. In particular, the two models presented here illustrate 1) that THz switching is possible, 2) that device design choices like the location of the actuating electrode can influence switching speed, and 3) that fully-coupled magnetomechanical models are necessary to predict the frequency response of strain-controlled antiferromagnets. The results presented here do not mandate that realistic devices be limited to

frequencies far below antiferromagnetic resonance. For example, reducing an antiferromagnet's dimension in the direction of mechanical wave propagation should increase operational frequency. Since an antiferromagnet's thickness is commonly its shortest dimension, co-locating the actuating electrode underneath it may increase switching speed up to 20 x.

Furthermore, the energy required to operate at these frequencies can be low. The energy cost per state switch was calculated from the model by numerically integrating the applied charge density over the electrode surface and then using $E_{switch} = QV/2$ to find the energy stored capacitively in the piezoelectric layer. We found that 450 aJ was sufficient to switch axis of antiferromagnetic alignment 90˚. This is 3 orders of magnitude more energy efficient than alternative magnetic control methods, like spin transfer torque, which requires 100 fJ/state switch [33].

4.4 Considerations Regarding Shape, Symmetry, and Ground States

So far, the developed model has been used to consider 90˚ switching either from out-of-plane to in-plane, or between in-plane axes. This was done only for circular antiferromagnetic bits and square straining electrodes. These shapes were chosen because other trial simulation results showed a heavy dependence on the strain pulse wavefront geometry and symmetry breaking in the antiferromagnetic bit.

Since the antiferromagnetic bits considered here exhibit low intrinsic anisotropy (i.e. low MCA), the magnetostriction dominates the ground state formation and, thus, the ground state is ultimately dictated by shear lag effects occurring at the geometry edges. These effects arise when strain in thin structures relaxes at the geometry walls, creating high strain gradients at the edges and a relaxed strain state everywhere else [12]. In the case where these strains are coupled to antiferromagnetic spins, Néel vectors in a single domain that are initialized out-of-plane tend to

cant inwards at the geometry edges. In this disk used for the previous studies, the inward canting resulted in a meta-stable state at the disk center, where one Néel vector points exactly out-of-plane, and all the surrounding vectors point slightly towards the center. From here, any small fluctuations of these near-center Néel vectors are sufficient to break the circular symmetry and relax the system into a chiral state. An example is shown in Figure 4.5, below.

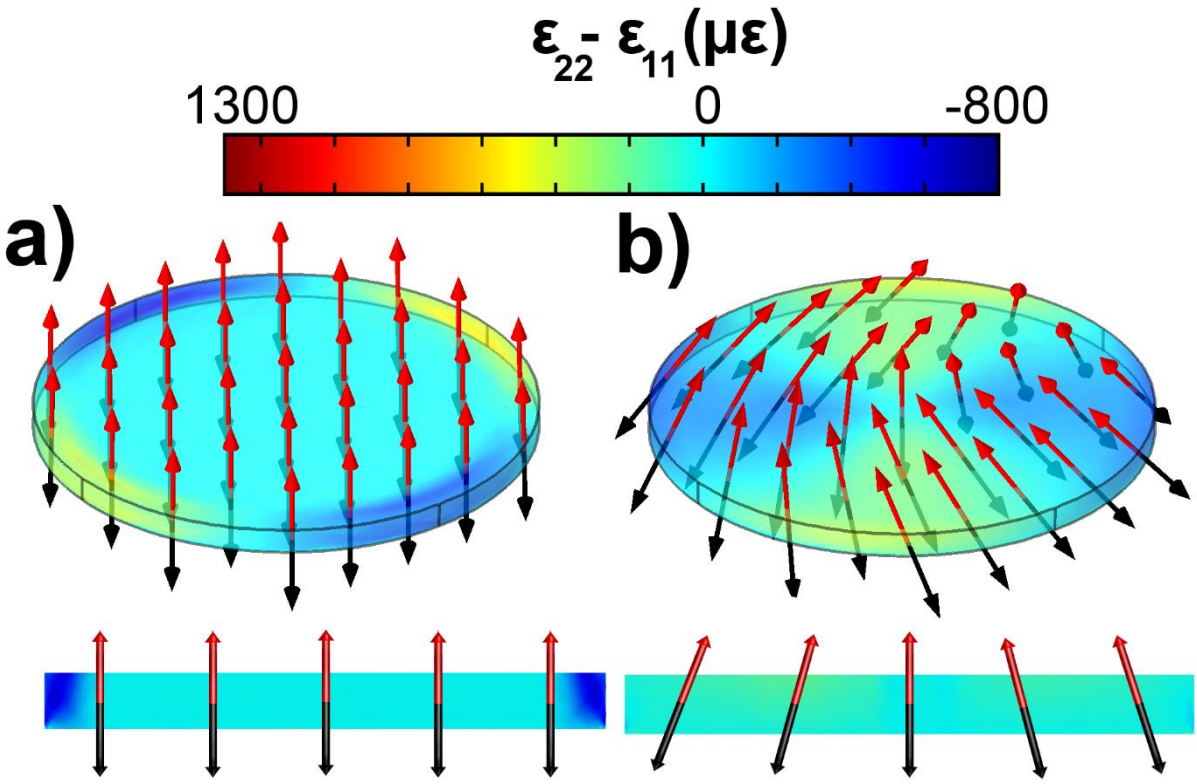

Figure 4.5 – (a) the initialized out-of-plane state is shown, with cross-section view below. (b) the relaxed state and cross-section is shown, highlighting the Néel vector canting at the geometry edges and broken circular symmetry with the Néel vector wrapping around the geometry center with a right-to-left twist.

Since the geometry shown in Figure 4.5(b) is a disk, any impinging acoustic plane wave will reach a single point at the edge of the disk first. At this point, the Néel vector will be locally rotated in-plane when the acoustic wave arrives. Specifically, the rotation will occur towards the center of the disk, since the shear lag effects dictate that this is the closest new easy axis. As a result, the

neighboring Néel vectors will also rotate in-plane due to exchange coupling. The chiral spin structure in Figure 4.5(b) guarantees that, as the neighbors rotate, they will reach the in-plane orientation with an asymmetric left-to-right canting, as shown in the right half of Figure 4.6, below.

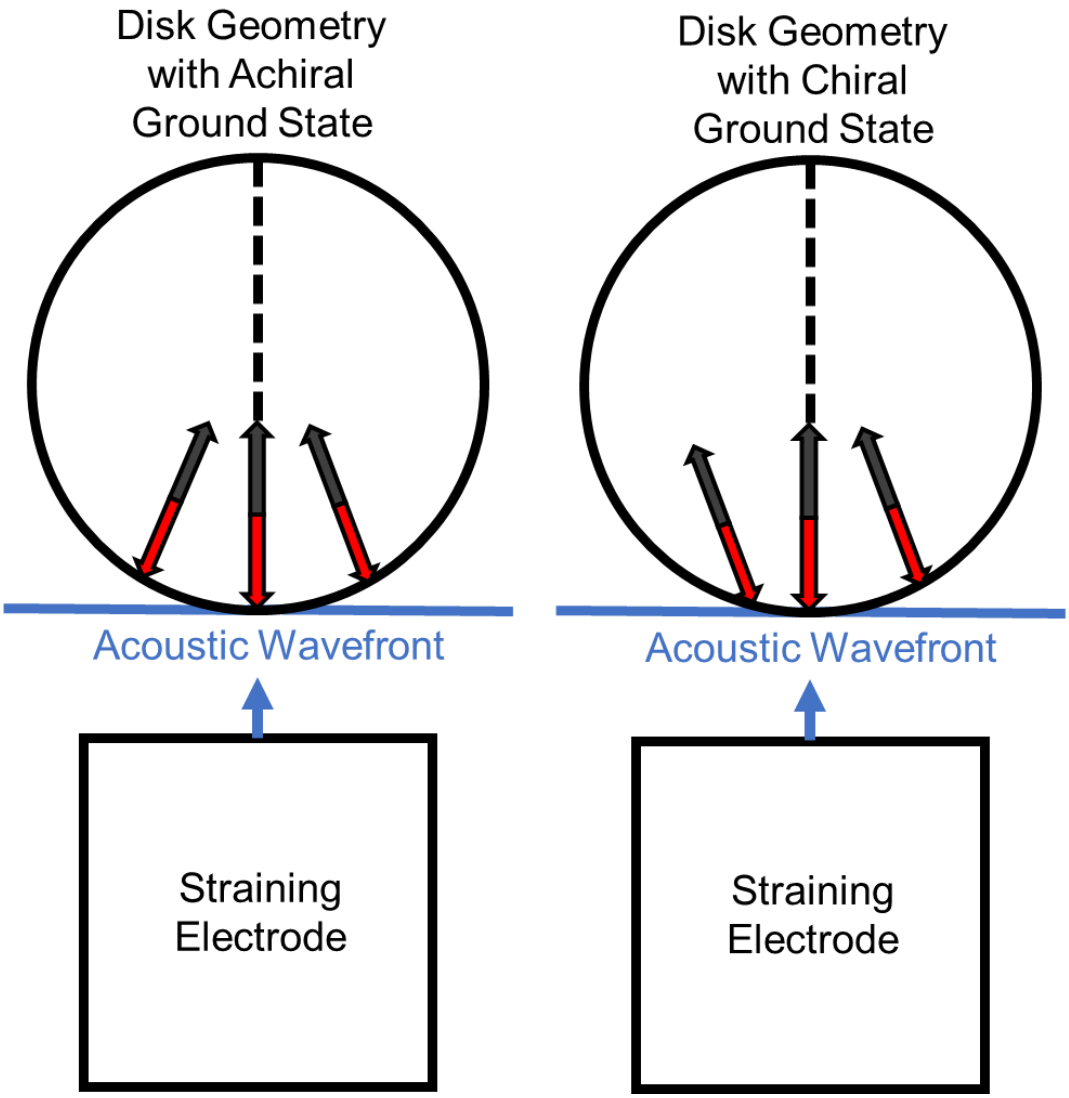

Figure 4.6 – (Left) As an acoustic wave arrives at the edge of an antiferromagnetic disk, it rotates the local Néel vector in-plane, dragging the neighbors with it. If the disk was initialized out-of-plane and relaxed to have center-symmetric shear lag effects, this will cause the neighbors to cant towards each other, leading to a 2-domain state (Right) If the spin structure is initially relaxed into a chiral state, like in Figure 4.5(b), the motion of the first Néel vector will cause the neighbors to move in-plane without fighting the exchange anisotropy.

Without the chiral spin structure, the Néel vectors to the right and left of the acoustic wave's arrival location would cant towards each other, as shown in the left half of Figure 4.6. This would result in a 2-domain state and, therefore, non-deterministic switching. Such a state would also yield little change in the magnetoresistance, and thus be less useful for memory applications.

To describe this problem in more detail, some cases are examined that depend not only on the initial spin structure but also on the antiferromagnet geometry. In particular, the disk shape was replaced by a square antiferromagnet, and the same switching study (i.e. with an acoustic plane wave from a nearby square electrode) was repeated. The initial state for the square was similar to the disk – it starts uniformly out-of-plane and relaxes to a chiral shear lagged state where the Néel vector along the edges cants towards the center of the square, as shown from top-down view in Figure 4.7.

For the square geometry, the Néel vector in the corners is always seen to point towards the square's center. Due to the higher shear lag effects in the corners, these Néel vectors are effectively pinned.

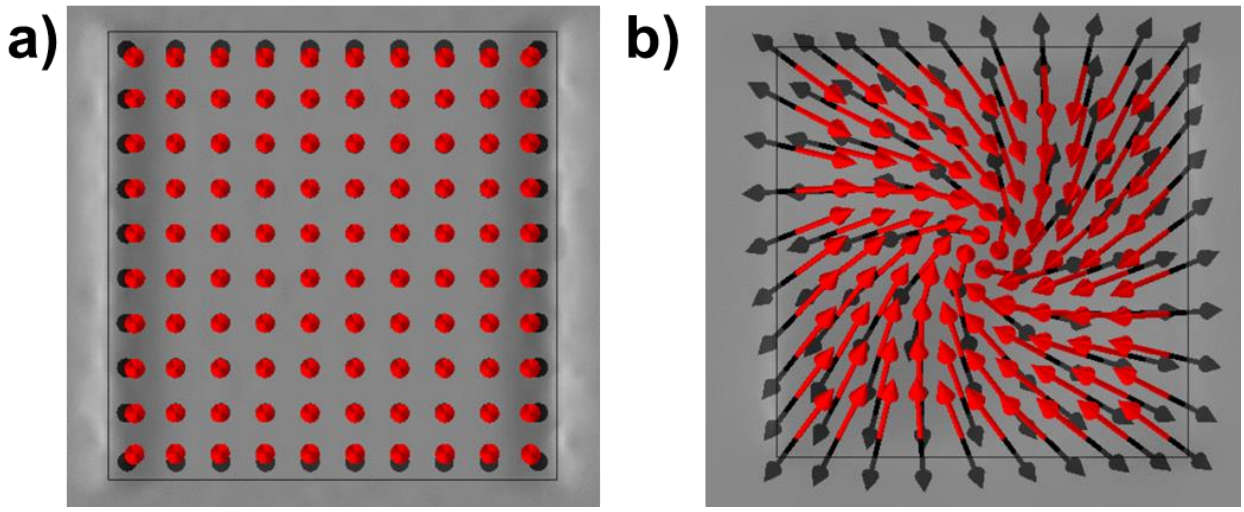

Figure 4.7 – (a) the initialized out-of-plane orientation for the square geometry is shown. (b) the relaxed chiral state of the square is shown. One important difference with the disk in Figure 4.5 is that the square geometry always results in center-pointing Néel vectors in the square's corners.

As a result, the overall chiral spin structure in the interior of the square does not dominate the switching dynamics, the pinned Néel vectors in the corners do. To make this evident, Figure 4.8 shows the antiferromagnetic state at an early state in the switching, when the straining wavefront (dark blue is compressive strain, light blue is near 0 strain) is about half way across the length of the square. The figure shows that the Néel vectors on the left- and right-hand sides of the square cant inwards, resulting in a 2-domain "mohawk" state, with a central out-of-plane domain wall.

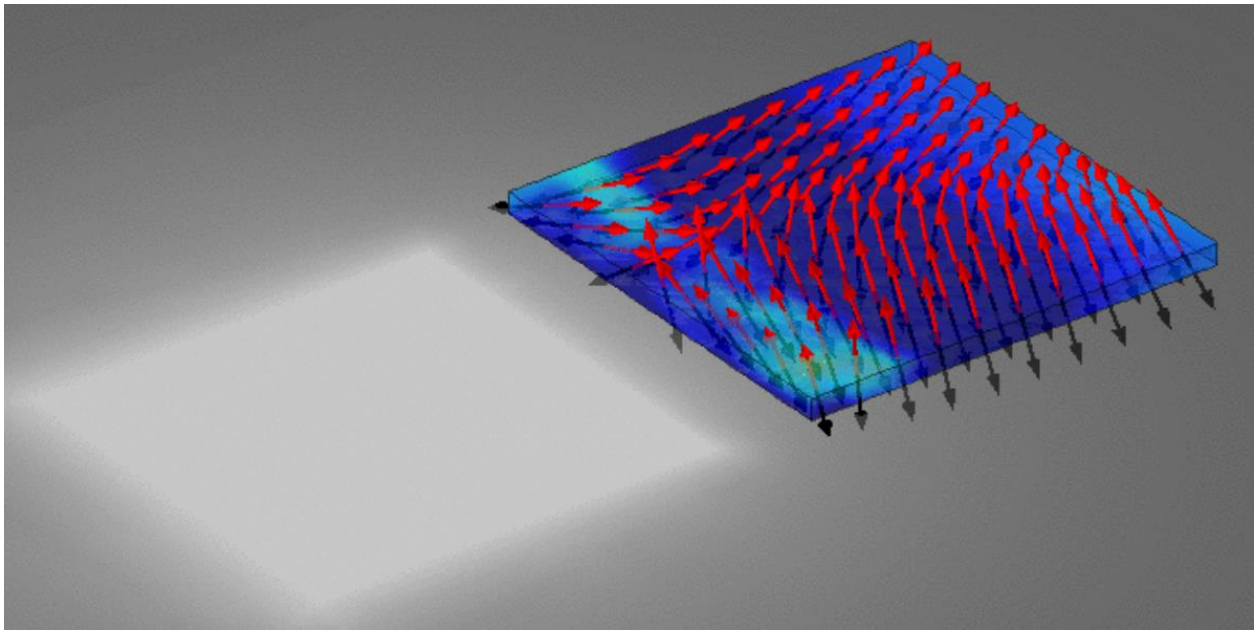

Figure 4.8– The magnetically relaxed square in Figure 4.7(b) is strained via an acoustic wave excited at a neighboring electrode (white square), inducing about 750με of compression that passes through the square dynamically. The Néel vector on the left and right hand sides of the square cant inwards, resulting in a 2-domain state with an out-of-plane domain wall.

From this result, it is clear that two conditions benefit switching in single domain antiferromagnets with shear lagged relaxed states: (i) the strain wavefront should impinge upon the bit at a single point, and (ii) a projection of the bit's relaxed spin structure onto the strain-induced easy axis should break central symmetry.

One important consequence of these conditions is that the common 2-electrode design for local strain-switching of ferromagnets in multiferroic composites (see Figure 2.1) is not optimal for antiferromagnets. If electrodes on both sides of an antiferromagnetic bit were actuated together, they would cant both sides of the bit towards the center, again resulting in a 2-domain state.

4.4. Conclusion

In conclusion, a fully-coupled finite element model incorporating micromagnetics, elastodynamics, and piezoelectricity was developed to predict voltage-induced magnetoelastic switching behavior in antiferromagnets. Results demonstrated that the frequency of antiferromagnetic switching can approach THz, but the speed is influenced by the transient of the mechanical excitation. For this reason, special attention should be paid to the antiferromagnetic bit geometry and mechanical impedance matching between the bit and the substrate. Even with a non-optimized system, the developed model predicted an energy cost for strain-switching of antiferromagnets to be extremely low (on the order of 100's of aJs). This combination of high speed and low power control may offer a new development avenue for next generation memory devices.

The developed model was also used to analyze unique effects for antiferromagnets. This included finding cases where the strain interacts heavily with the geometry of the magnetic bit to influence switching in ways that are not possible with ferromagnets. Specifically, the model predicts that shear lag is more important in antiferromagnets than in ferromagnets and, in fact, dominates the ground state formation. This is predicted here for the first time. If the model is correct, the magnetic edge states of an antiferromagnetic single domain may differ substantially from the rest of the domain structure, resulting in switching behavior that depends completely on the edge states. To test this, the model was used to first calculate ground states in disks and squares (both with a Néel

vector initialized out-of-plane), and then strain them via a neighboring electrode. This caused switching in the disk-shaped antiferromagnetic bits but indeterminant 2-domain formation in square-shaped bits. Some rules are suggested by the author for improving the likelihood of deterministic switching in magnetoelastic antiferromagnets.

In the following section, the concept of strain-induced magnetic anisotropy in antiferromagnets is developed further by experimentally testing a similar system to those modeled here.

4.5. Chapter References

[1] Q. Wang *et al.*, "Strain-mediated 180?? switching in CoFeB and Terfenol-D nanodots with perpendicular magnetic anisotropy," *Appl. Phys. Lett.*, vol. 110, no. 10, pp. 1–6, 2017.

[2] N. D'Souza, M. Salehi Fashami, S. Bandyopadhyay, and J. Atulasimha, "Experimental Clocking of Nanomagnets with Strain for Ultralow Power Boolean Logic," *Nano Lett.*, vol. 16, no. 2, pp. 1069–1075, 2016.

[3] Y. Mukai, H. Hirori, T. Yamamoto, H. Kageyama, and K. Tanaka, "Terahertz Nonlinear Magnetic Response in Antiferromagnets," *Proc. CLEO 2015*, vol. 1, no. c, pp. 4–5, 2015.

[4] H. Kondoh, "Antiferromagnetic Resonance in NiO in Far-infrared Region," *J. Phys. Soc. Japan*, vol. 15, no. 11, pp. 1970–1975, 1960.

[5] L. Alberts and E. W. Lee, "Magnetostriction in Antiferromagnetic Nickel Oxide," *Proc. Phys. Soc.*, vol. 78, pp. 728–733, 1961.

[6] J. P. Domann, W. Y. Sun, L. T. Schelhas, and G. P. Carman, "Strain-mediated multiferroic control of spontaneous exchange bias in Ni-NiO heterostructures," *J. Appl. Phys.*, vol. 120, no. 14, 2016.

[7] A. He, T. Ma, J. Zhang, W. Luo, and M. Yan, “Antiferromagnetic Mn50Fe50 wire with large magnetostriction,” *J. Magn. Magn. Mater.*, vol. 321, no. 22, pp. 3778–3781, 2009.

[8] C.-Y. Liang *et al.*, “Modeling of magnetoelastic nanostructures with a fully coupled mechanical-micromagnetic model,” *Nanotechnology*, vol. 25, no. 43, p. 435701, 2014.

[9] J. X. Zhang and L. Q. Chen, “Phase-field model for ferromagnetic shape-memory alloys,” *Philos. Mag. Lett.*, vol. 85, no. 10, pp. 533–541, 2005.

[10] J. M. Hu, G. Sheng, J. X. Zhang, C. W. Nan, and L. Q. Chen, “Phase-field simulation of strain-induced domain switching in magnetic thin films,” *Appl. Phys. Lett.*, vol. 98, no. 11, pp. 88–91, 2011.

[11] X. Li *et al.*, “Strain-mediated 180° perpendicular magnetization switching of a single domain multiferroic structure,” *J. Appl. Phys.*, vol. 118, no. 1, 2015.

[12] C. Y. Liang *et al.*, “Electrical control of a single magnetoelastic domain structure on a clamped piezoelectric thin film - Analysis,” *J. Appl. Phys.*, vol. 116, no. 12, pp. 0–9, 2014.

[13] J. Cui *et al.*, “A method to control magnetism in individual strain-mediated magnetoelectric islands,” *Appl. Phys. Lett.*, vol. 103, no. 23, 2013.

[14] H. Sohn *et al.*, “Electrically driven magnetic domain wall rotation in multiferroic heterostructures to manipulate suspended on-chip magnetic particles,” *ACS Nano*, vol. 9, no. 5, pp. 4814–4826, 2015.

[15] C. Chen, A. Barra, A. Mal, G. Carman, and A. Sepulveda, “Voltage induced mechanical/spin wave propagation over long distances,” *Appl. Phys. Lett.*, vol. 110, no. 7, 2017.

[16] Y. G. Semenov, X. L. Li, and K. W. Kim, "Currentless reversal of Néel vector in antiferromagnets," *Phys. Rev. B - Condens. Matter Mater. Phys.*, vol. 95, no. 1, pp. 1–6, 2017.

[17] D. Suess, T. Schrefl, W. Scholz, J. V. Kim, R. L. Stamps, and J. Fidler, "Micromagnetic simulation of antiferromagnetic/ferromagnetic structures," *IEEE Trans. Magn.*, vol. 38, no. 5 I, pp. 2397–2399, 2002.

[18] D. Suess, M. Kirschner, T. Schrefl, J. Fidler, R. L. Stamps, and J.-V. Kim, "Exchange bias of polycrystalline antiferromagnets with perfectly compensated interfaces," *Phys. Rev. B*, vol. 67, no. 5, p. 54419, 2003.

[19] P. Miltényi *et al.*, "Diluted Antiferromagnets in Exchange Bias: Proof of the Domain State Model," *Phys. Rev. Lett.*, vol. 84, no. 18, pp. 4224–4227, 2000.

[20] U. Nowak, A. Misra, and K. D. Usadel, "Domain State Model for Exchange Bias," *J. Appl. Phys.*, vol. 89, no. 11, p. 8, 2000.

[21] G. T. Rado, "Mechanism of the magnetoelectric effect in an antiferromagnet," *Phys. Rev. Lett.*, vol. 6, no. 11, pp. 609–610, 1961.

[22] G. T. Rado and V. J. Folen, "Observation of the Magnetically Induced Magnetoelectric," vol. 7, no. 8, pp. 310–311, 1961.

[23] N. Wu *et al.*, "Imaging and control of surface magnetization domains in a magnetoelectric antiferromagnet," *Phys. Rev. Lett.*, vol. 106, no. 8, pp. 17–20, 2011.

[24] F. Máca *et al.*, "Room-temperature antiferromagnetism in CuMnAs," *J. Magn. Magn. Mater.*, vol. 324, no. 8, pp. 1606–1612, 2012.

[25] M. J. Grzybowski *et al.*, “Imaging Current-Induced Switching of Antiferromagnetic Domains in CuMnAs,” *Phys. Rev. Lett.*, vol. 118, no. 5, pp. 1–5, 2017.

[26] R. C. O’handley, *Moden Magnetic Materials: Principles and Applications*. 2000.

[27] C. Kittel, “Theory of Antiferromagnetic Resonance,” *Phys. Rev.*, vol. 85, no. 2, p. 565, 1952.

[28] A. Vansteenkiste and B. Van De Wiele, “MuMax: A new high-performance micromagnetic simulation tool,” *J. Magn. Magn. Mater.*, vol. 323, no. 21, pp. 2585–2591, 2011.

[29] J. Du Shiming Zhou, Li Sun, “Exchange Bias Material: FeMn,” *Handb. Spintron.*, pp. 253–281, 2016.

[30] T. Ma, J. Zhang, A. He, and M. Yan, “Improved magnetostriction in cold-rolled and annealed Mn50Fe50 alloy,” *Scr. Mater.*, vol. 61, no. 4, pp. 427–430, 2009.

[31] J. T. Lenkkeri, “Measurements of elastic moduli of face-centred cubic alloys of transition metals,” *J. Phys. F Met. Phys.*, vol. 11, no. 10, pp. 1991–1996, 1981.

[32] J. Hong, B. Lambson, S. Dhuey, and J. Bokor, “Experimental test of Landauers principle in single-bit operations on nanomagnetic memory bits,” *Sci. Adv.*, vol. 2, no. 3, pp. e1501492–e1501492, 2016.

[33] K. L. Wang, J. G. Alzate, and P. Khalili Amiri, “Low-power non-volatile spintronic memory: STT-RAM and beyond,” *J. Phys. D. Appl. Phys.*, vol. 46, no. 7, p. 74003, 2013.

[34] Navabi, Aryan, et al. "Efficient Excitation of High-Frequency Exchange-Dominated Spin Waves in Periodic Ferromagnetic Structures." *Physical Review Applied* 7.3 (2017): 034027.

[35] Sohn, Hyunmin, et al. "Electrically driven magnetic domain wall rotation in multiferroic heterostructures to manipulate suspended on-chip magnetic particles." *ACS nano* 9.5 (2015): 4814-4826.

[36] Gilbert, Ian, et al. "Magnetic microscopy and simulation of strain-mediated control of magnetization in PMN-PT/Ni nanostructures." *Applied physics letters* 109.16 (2016): 162404.

[37] Alberts, L. & Lee, E. W. "Magnetostriction in Antiferromagnetic Nickel Oxide." *Proceedings of the Physical Society,* **1961**, *78*, 728.

[38] Plessis, P.-d.-V. d.; Tonder, S. J. v. & Alberts, L. "Magnetostriction of a NiO single crystal. II." *Journal of Physics C: Solid State Physics,* **1971**, *4*, 2565.

[39] Yamada, T.; Saito, S. & Shimomura, Y. "Magnetic Anisotropy, Magnetostriction, and Magnetic Domain Walls in NiO. II. Experiment." *Journal of the Physical Society of Japan,* **1966**, *21*, 672-680.

[40] McGuire, T. R. & Crapo, W. A. "Magnetic Susceptibility and Magnetostriction of CoO, MnO, and NiO." *Journal of Applied Physics,* **1962**, *33*, 1291-1292.

[41] Gilbert, Thomas L. "A Phenomenological Theory of Damping in Ferromagnetic Materials." *IEEE Transactions on Magnetics* 40.6 (2004): 3443-3449.

[42] Coey, John M.D. *Magnetism and Magnetic Materials*. Cambridge University Press, 2010.

[43] Gopman, Daniel B., et al. "Determination of the exchange constant of Tb 0.3 Dy 0.7 Fe 2 by broadband ferromagnetic resonance spectroscopy." *Physical Review B* 93.6 (2016): 064425.

[44] Barangi, Mahmood, and Pinaki Mazumder. "Straintronics-based magnetic tunneling junction: Dynamic and static behavior analysis and material investigation." *Applied Physics Letters* 104.16 (2014): 162403.

V. Magnetic Memory with Antiferromagnets: Experimental Feasibility Study

5.1. Introduction

As previously mentioned, antiferromagnets offer a number of advantages compared to ferro- or ferrimagnets: their resonances are 10-100 times higher (supporting THz dynamics), and their lack of magnetic moment makes them both resistant to magnetic noise and more densely packable in on-chip arrays.

While these features are very promising for MRAM, they are also ironically the main issues that are currently preventing antiferromagnets from being used. Their high resonances lie in the THz bandgap, which makes them difficult to excite electrically or optically, and their lack of moment makes their magnetic orientation hard to detect or control. As a result, there are currently no known approaches for reading or writing antiferromagnetic memory that are both energy efficient and scalable.

For the read step, the only available method that can be used on-chip is spin Hall magnetoresistance (SMR) [1]. SMR involves layering a heavy metal (HM) exhibiting strong spin orbit interaction with an antiferromagnet. In this configuration, charge currents passed in the plane of the HM are converted into spin currents in the out-of-plane direction due to the spin Hall effect (SHE). When the out-of-plane spin current encounters a HM interface, it is scattered back, reversing the spin current and also generating a backwards charge current due to the inverse SHE. At the HM-antiferromagnet interface, the reflection of the spin current depends on the spin current's polarization angle and the antiferromagnetic order parameter, the Neél vector (defined $n = m_1 - m_2$). If the Neél vector and charge current lie on the same axis, the reflected spin current increases the HM resistance, and if they are orthogonal, the resistance

is lowered. By this method, the Neél vector orientation can be read as a magnetoresistive memory state variable.

For the write step, there are three established options: magnetic field [2], current (e.g. spin orbit or spin transfer torque) [3], or optical torque (via lasers) [4]. However, none of these are energy efficient or scalable. The magnetic field option competes with the antiferromagnetic exchange energy, resulting in sublattice canting and no Neél vector switching below the spin flop transition (> 1 Tesla). Alternatively, the current-based option offers on-chip switching but suffers from resistive heating that makes it inefficient. The final option, optical control, is promising for THz switching, but is again off-chip, and the laser systems used are large and power intensive. As a result, the search for a low power and scalable writing alternatives is still active.

In this section, we propose and experimentally examine mechanical strain and SMR as new combination for efficient and scalable reading and writing in antiferromagnetic MRAM. Unlike field-induced unidirectional anisotropy, strain is uniaxial, which allows free Neél vector rotation that does not compete with the antiferromagnetic exchange energy. In addition, strain control is achievable on-chip by layering magnetoelastic and piezoelectric films into composites (i.e. multiferroics), whose strain state can then be modified by applying a voltage across the piezoelectric layer's thickness. Since this approach utilizes high voltage but low current, it dissipates 100-1000 times less power (aJs per state switch [5]) than spin transfer torque and also scales favorably with shrinking device area.

Despite the beneficial aspects of this approach, little has been done to characterize the magnetoelastic strain response of antiferromagnets, especially in thin films. One possible reason is that, while strain anisotropy can easily be identified by a shift in coercive field for ferromagnets, no equivalent test exists for antiferromagnets. Excluding the SMR method

previously mentioned, the Neél vector is not identifiable outside of x-ray or neutron beamline facilities, which makes magnetostrictive testing costly and difficult.

Despite these challenges, there is at least one antiferromagnet that has previously been reported to exhibit both magnetostriction and SMR: single-crystal [111] NiO. Its SMR (with Pt HM layer) was recently measured to be on the order of 10^{-5} [6], and its saturation magnetostriction ($\lambda_s = 26 \times 10^{-6}$) [7] is similar to Ni, making it promising for strain-mediated MRAM. To make it fully relevant for device applications, however, a method is needed to overcome its strong magnetocrystalline (111) easy-planes [8], since they make it difficult to do in-plane switching of the form commonly used in magnetic tunnel junctions.

The easiest way to avoid such magnetocrystalline pinning is to eliminate the crystalline structure entirely by switching to polycrystalline NiO. In this case, the material should become nearly isotropic, since the MCA is typically reduced by 2-5 orders of magnitude for polycrystals [9][10]. This would not only solve the pinning problem, but also lower the energy cost for switching, making it highly desirable. However, by changing the long-range material order, two complex competing effects are also generated, which so far have gone unresearched. The first is that magnetostriction is usually decreased in polycrystals; for NiO, this decrease is about a half an order of magnitude, to $\lambda_s = 6 \times 10^{-6}$ [11]. This may prohibit the generation of sufficient strain anisotropy to accomplish magnetic switching even in the absence of MCA. The second is that the SMR amplitude may be highly sensitive to the long-range order, making it impossible to read strain-written states in polycrystalline antiferromagnets. Currently, there has been no analysis on this complicated trade-off between reduced MCA or magnetostriction, and it is not known whether SMR can be measured in polycrystalline antiferromagnets. To address these issues, this paper presents a novel measurement of SMR in polycrystalline NiO, and further demonstrates that the measured SMR amplitude can be strain-tuned as a potential first step towards quantifying magnetoelastic anisotropy in antiferromagnets.

5.2. Experimental Methods

To examine the strain response of polycrystalline NiO via SMR, a multiferroic composite containing layered NiO and Pt (as a HM layer) was prepared on a 1x1 cm, 500 µm-thick [011]-cut single crystal piezoelectric $PbMg_{1/3}Nb_{2/3}O_3$-$PbTiO_3$ (PMN-PT) substrate. [011]-cut PMN-PT was selected because it generates anisotropic in-plane strain (tension along [010] and compression along [100]) when positive out-of-plane electric field is applied, making it ideal for maximizing the biaxial strain (ε_{yy}- ε_{xx}) that controls magnetic anisotropy. To minimize any remanent stresses and ensure a linear piezoelectric response, the PMN-PT was electrically poled before NiO deposition. Poling proceeded by applying an out-of-plane electric field of 0.8 MV/m with positive voltage at the back surface electrode and electrical ground at the top surface electrode. This same top surface electrode also served as the base of the antiferromagnetic-HM stack, which comprised a 5 nm Ti/60 nm Au adhesion layer followed by a Pt/NiO/Pt stack, with thicknesses of 30 nm, 7 nm, and 3 nm, respectively. Each of these layers were deposited via electron-beam evaporation at a base pressure of 10^{-6} Torr, following a process that is known to grow polycrystalline NiO free from Ni_2O_3 or $Ni(OH)_2$ defects [12]. The antiferromagnetic character of the as-grown film was confirmed first by magnetometry, using a superconducting quantum interference device (SQUID), and later by measuring an absence of x-ray magnetic circular dichroism (XMCD).

The finished films were patterned into H-shaped Hall bars, each surrounded laterally by two rectangular Au contacts for strain application, as shown in Figure 1. Fabrication was accomplished using a two-step optical lithography process with Ar reactive ion etching (RIE) for Hall bar definition (800 W for 1.5 minutes) and subsequent lift-off with a negative tone photoresist (nLOF 2020) for surrounding contact definition.

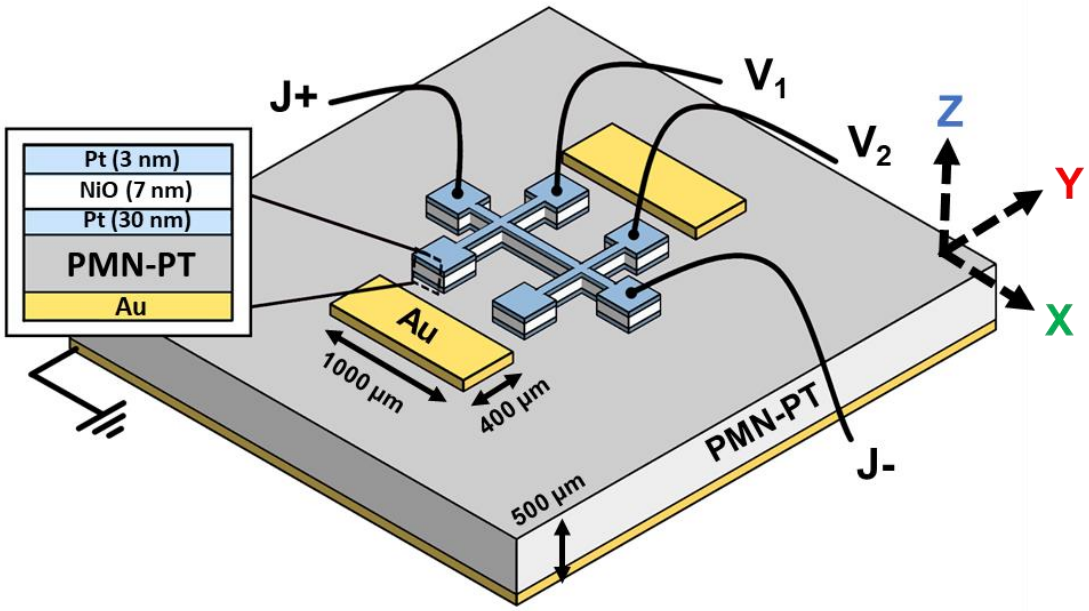

Figure 5.1 – The device structure is shown, with NiO/Pt Hall bar at center, and straining electrodes on the sides.

The chosen geometry from Figure 1 provided three benefits: (i) the Hall bar configuration enabled longitudinal resistance measurement in the standard 4-point probe configuration, (ii) the placement of the straining electrodes away from the Hall bar negated any magnetoelectric contribution to the magnetic anisotropy, and (iii) the micron scale and individually addressable devices made the structure particularly relevant for technological applications.

The patterned devices were contacted via Al wire-bonding to printed circuit board sample holders that allowed for simultaneous current passage down the length of the Hall bar, longitudinal SMR resistance measurement at the H-shaped contacts, and high voltage application at the neighboring Au pads for substrate straining. All currents and high voltages

(for strain application) were sourced by Keithley 2400 Sourcemeters operating in either current or voltage source mode, and the SMR voltages were measured with a Keithley 2182A Nanovoltmeter. During strain application, negative voltage was supplied to the patterned top surface electrodes, and the back side of the substrate was grounded (providing an electric field that matches the initial poling direction). In this configuration, the top surface electrodes should

experience out-of-plane displacements that are linear with electric field and generate in-plane biaxial tension perpendicular to the Hall bar axis. The magnitude of the biaxial strains for each applied straining voltage were estimated using a piezoelectric finite element simulation and appeared to be roughly uniform in the central region of the Hall bar (see inset of Figure 1).

Since the Pt HM layer is particularly sensitive to temperature and strain, all measurements were performed in an 11 T cryostat with heater coils in the sample space for active temperature control. The sample space was maintained at 200 ± 0.01 K for at least 20 minutes prior to every measurement, thereby ensuring that there would be no temperature-derived changes in sample resistance or thermomechanical strain state.

To complete the full study, SMR was measured as both a function of strain and externally applied magnetic field (applied via the Helmholtz coil in the cryostat). At each strain and magnetic field condition, the SMR contribution to the total resistance was identified by alternating the current direction, maintaining the current for 15 seconds (to eliminate ohmic heating transients), and then computing the average sum of the resistances for both current directions. This process was repeated 15 times for each of the two current directions to improve the SMR measurement statistics.

Following this approach, two types of measurements were conducted. In the first, SMR was confirmed in polycrystalline NiO/Pt following the same procedure used to characterize SMR in [111] NiO/Pt [13]. This involved rotation of the sample in 4 magnetic fields (using an Attocube ANRv1RES piezorotator) to find the angular-dependent SMR. In the second, strain effects were studied. Since theory dictates that strain should manifest in strictly uniaxial anisotropy changes, the sample was fixed for the second measurement (with $J \parallel H$), and an external magnetic field was swept from 0 T to 11 T along the Hall bar long axis. SMR was recorded at each 0.5 T increment. To determine the SMR's sensitivity to strain, this process was then repeated for 5 different tensile strains, each generated by applying 0 to 0.4 MV/m in 0.1 MV/m steps across

the PMN-PT. For this range of electric fields, the PMN-PT response should be nearly linear (i.e. hysteresis free), and should correspond to piezostrains in the range from 0 to 250 με in 65 με increments.

To verify that the applied voltages do, in fact, result in strain at the location of the NiO/Pt device, the resistance of the Pt layer was measured at 0 magnetic field for a variety of strain values (see Figure 5.2).

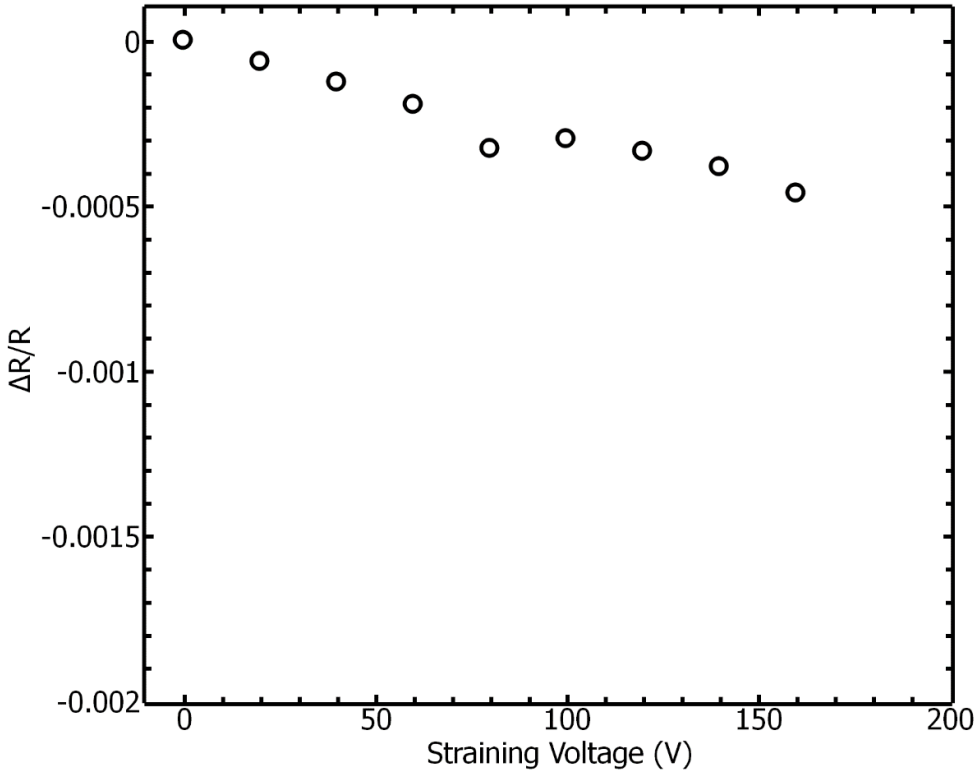

Figure 5.2 – The surface resistance of the Pt is plotted for multiple strain states while the magnetoresistance contribution is minimal (i.e. the external magnetic field is 0). The changes shown here correspond with piezoresistive changes in Pt.

Figure 5.2 shows a roughly linear change in the Pt resistance as more strain is applied, and the effective strain can be calculated by dividing the resistance change by the gage factor (GF) for platinum, which is likely around 3 at 200 K [14][15]. This yields a strain of 150 με at 150 V, within about 20% of the predicted value from the finite element calculation.

5.3. Results and Discussion

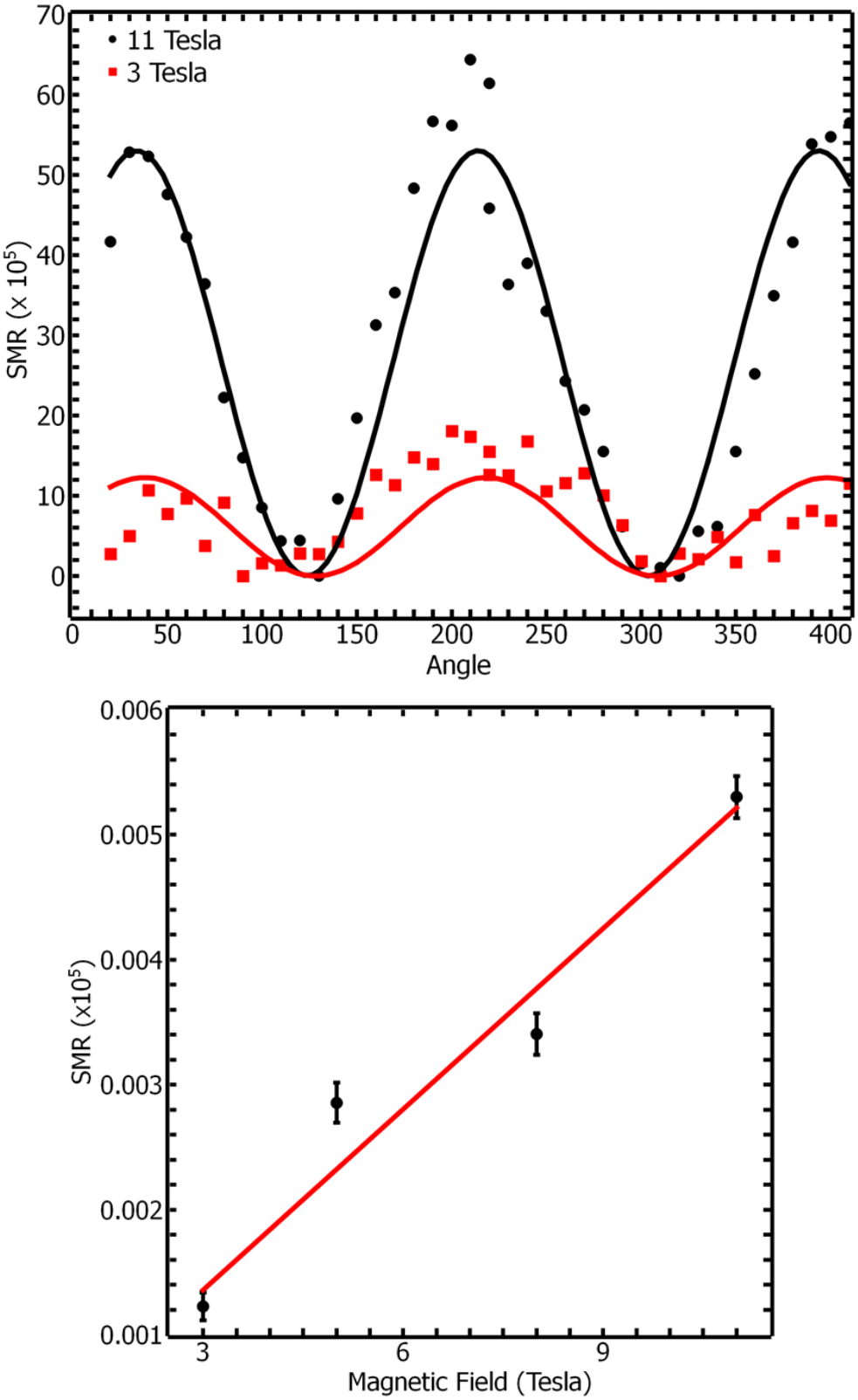

Figure 5.3 – (Top) The angle-resolved SMR of the NiO/Pt is shown for 11 T and 3 T, the maximal and minimal field cases considered here. (Bottom) The field dependence of the SMR amplitude is plotted for 4 field values, showing an appoximately linear increase with field. A fit line is shown in red, and the R^2 of the fit is 0.97.

A. Polycrystalline NiO-Pt Characterization by SMR

Figure 5.3(a) shows the angle-resolved SMR in polycrystalline NiO/Pt for 3 T (red O's) and 11 T (black X's). For both field conditions, the driving current used was 350 μA, and a full 420° of x-y plane SMR data was obtained by rotating the sample from 0 to 210°, inverting the magnetic field, and rotating back. Each dataset was corrected for thermal drift when present. Both datasets in Figure 1a exhibit a periodic change in resistance that characterizes the presence of antiferromagnetic SMR, with high resistance when $\mathbf{n} \parallel \mathbf{J}$ and low resistance when $\mathbf{n} \perp \mathbf{J}$. To extract the SMR amplitudes, the data was fit by least squares regression using functions of the form $\Delta R \sin^2(\alpha + \alpha_{0,xx})$, where α is the sample angle and ΔR is the normalized SMR amplitude, resulting in a largest ΔR of 57±2 x 10^{-6} for 11 T. This ΔR was only 15% less than the recently reported value for similar, but single-crystal, [111] NiO Hall bars with Pt HM layers [13], indicating that a lack of crystallographic order does not significantly influence NiO/Pt's SMR. This validates SMR as a magnetic state read-variable for the first time, specifically for the class of polycrystalline antiferromagnets. It also indicates that the SMR generated at insulating antiferromagnet-HM interfaces may be less dependent on the long-range magnetic order than is sometimes thought. The results support a previous finding that amorphous materials can also exhibit a large spin Hall angle [16]. From an MRAM perspective, the agnostic relation between SMR amplitude and crystalline order opens up entirely new material options for technologically relevant in-plane switching and switching energy barrier reduction, which warrants further research.

The angle-resolved SMR also gives a first view of the relative saturating behavior for polycrystalline versus single-crystal NiO thin films. Figure 5.3(b) shows the SMR magnitude as a function of applied field. As expected, the SMR amplitude grows with field as more domains align, but the approximately linear growth (about 50% growth for every 3 Telsa) indicates that the polycrystalline NiO, similar to single crystal NiO [13], does not magnetically

saturate by 11T. The lack of saturation at high field may be due to poor interfacial conditions [17], or may be driven by the more randomized spin structure in polycrystalline materials. Regardless, it is clear that, despite the sharp reduction in MCA offered by polycrystalline NiO, the remaining secondary anisotropies are still sufficient to stabilize a domain structure against high applied fields. It has been theorized that one of the dominating secondary anisotropies may be magnetostrictive in origin [18].

B. Strain Tuning of SMR

To see how the SMR is changed along a single axis under the influence of strain, Figure 5.4 provides the field-dependent SMR along the Hall bar long axis ($J \parallel H$) with 0 V and 200 V applied across the PMN-PT, creating biaxial tensions of 0 and 280 με, respectively. In both cases, the general shape of the SMR roughly matches the expected $\Delta R \sim H^2$ behavior for non-saturated collinear antiferromagnets [1]. The SMR amplitude, which is calculated by

$$\Delta R/R = \frac{R(11\,T) - R(0T)}{R(0\,T)}$$

is 8.66 x 10^{-5} when 200 V is used to strain the PMN-PT, compared with 5.67 x 10^{-5} in the unstrained state, which is a 52% increase due to strain. Despite being a relatively large change, similar to that observed in the field-dependent SMR when an additional 3 T of external field is applied, it is still less than the observed change under a full 90˚ rotation of the Neél vector at 11 T (as can be confirmed in the angle-resolved SMR from Figure 2a). This indicates that, even with polycrystalline NiO's infinitesimal MCA, the reduced magnetostriction is sufficient to prohibit complete in-plane switching. However, the 52% change in $\Delta R/R$ is still large, and therefore suggests that comparatively small changes in the magnetostrictive energy can produce prominent changes in domain structure. This result thereby supports the previously mentioned theory that magnetostriction dominates the domain formation. So, despite not observing full switching under 400 με in this experiment, the result suggests that the complicated interplay

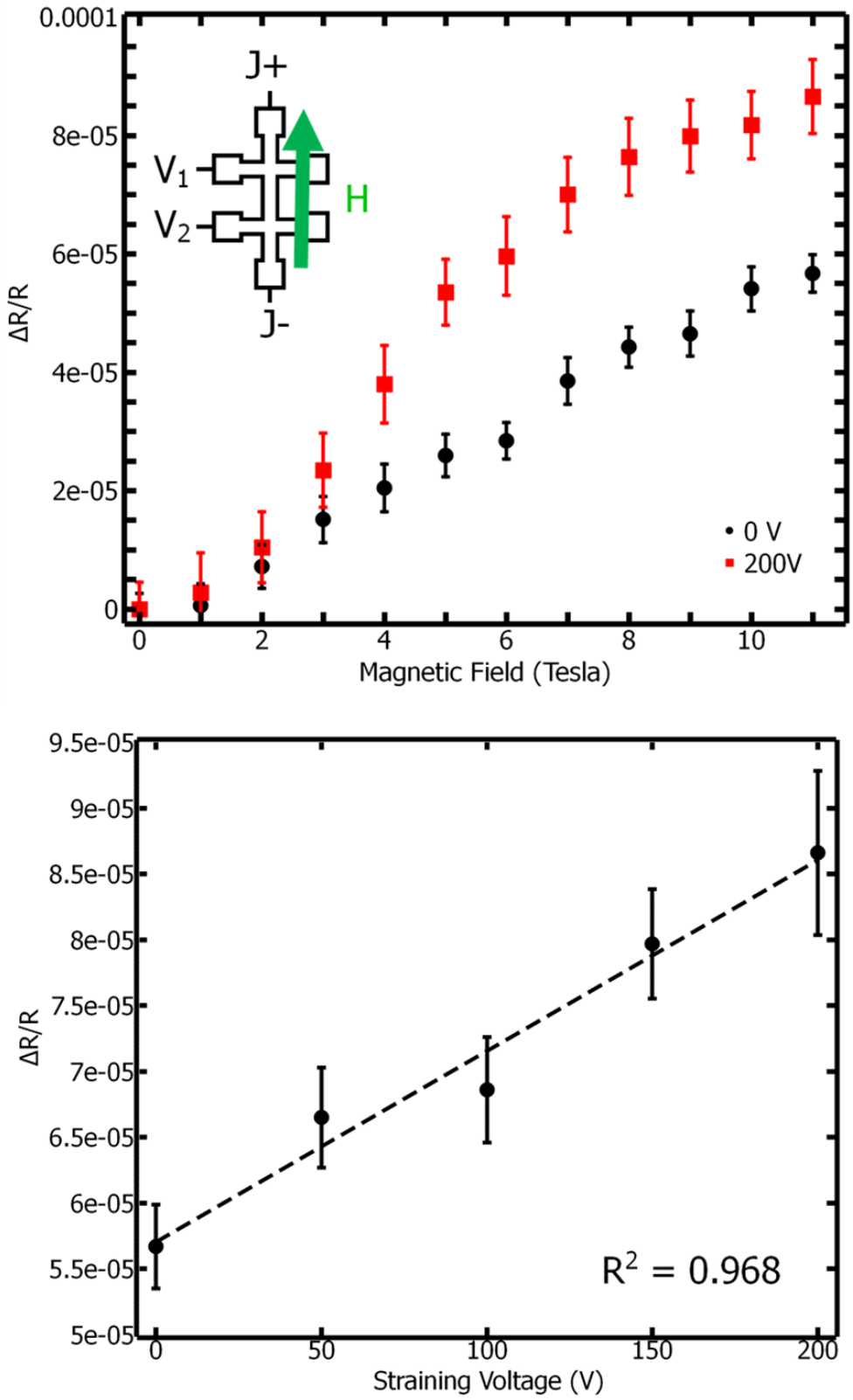

Figure 5.4 – (Top) The uniaxial SMR is plotted for the highest and lowest strain states. Higher strains result in higher SMR amplitudes at every field values. (Bottom) The SMR magnitude is plotted for 5 electrically-controlled strains, with 0 to 0.8 MV/m across the PMN-PT.

between reduced MCA and reduced magnetostriction in polycrystalline antiferromagnets may still favor magnetostrictive Neél vector control.

To quantify this effect, analyzing the change in $\Delta R/R$ at intermediate strain values (i.e. between the 0 and 400 με limits used in this experiment) is helpful. This range of strains was selected because they lie firmly within the linear piezoelectric and linear magnetoelastic regimes [19], meaning that repolarization of the PMN-PT can be ignored, and simple theory from ferromagnets can be used as a starting point to approximate the induced strain anisotropy value. The relevant theory for ferromagnets, in the absence of shear strains, predicts a linear change in induced magnetoelastic anisotropy with increasing biaxial strain that follows

$$H_{ME} \sim \frac{2B_1(\varepsilon_{yy} - \varepsilon_{xx})}{\mu_0 M_s}$$

where $B_1 = -\frac{15}{4}\lambda_s(C_{11} - C_{12})$ is defined as the magnetoelastic coefficient (and $C_{11} = 270$ GPa and $C_{12} = 170$ GPa [c] are the components of the elasticity matrix), $\varepsilon_{yy} - \varepsilon_{xx}$ is the biaxial strain, μ_0 is the permeability of free space, and M_s is the saturation magnetization. This equation is not expected to hold for antiferromagnets but is provided here only to support the proposition that, in the small strain limit, it is reasonable to expect that antiferromagnets may also exhibit magnetoelastic anisotropy that is linear in applied strain. This proposition is further supported by the bottom of Figure 5.4, which shows the change in $\Delta R/R$ for 0, 50, 100, 150, and 200 V applied across the PMN-PT. The observed change in $\Delta R/R$ is linear, which might indicate that the induced anisotropy follows an unknown linear theory. Additional evidence is provided here by the matching signs of NiO's magnetostriction and the observed direction of the change in $\Delta R/R$ in Figure 3b. The increasing strains applied in Figure 3b all produce tension on the axis perpendicular to the Hall bar and compression on the parallel axis. Consequently, this is expected to create a new magnetic easy-axis parallel to the Hall bar since NiO is negatively magnetostrictive. This interpretation is supported by the results since, at higher strain

levels, the observed $\Delta R/R$ is larger for the same applied magnetic field, implying a larger Neél vector rotation with field. In other words, the magnetic susceptibility along the Hall bar axis appears to increase, and this increase appears linear in strain.

To further quantify this effect, the linearized theory for ferromagnets can be used as a starting point. When the above equation is applied to a single Ni sublattice within polycrystalline NiO, using the reduced λ_s of 6 x 10^{-6}, and sublattice M_s of bulk Ni, then the implied magnetoelastic effective field is around 3100 Oe for 400 με of biaxial tension. Since Figures 1b and 3b show that application of 280 με and 3 T produce similar changes in $\Delta R/R$, it is possible that the Zeeman energy from the canted moment at 3T is similar to the magnetostrictive energy at 280με.

5.4. Conclusion

This paper proposed and experimentally examined the feasibility of a new form of electrically-controlled, strain-actuated antiferromagnetic memory based on multiferroic composites. The proposed memory system relied on SMR in an adjacent HM layer as a Neél vector read-out mechanism and strain anisotropy as a switching mechanism. To prove both concepts and maximize the experiment's technological relevance, the authors focused on polycrystalline NiO/Pt as a candidate material system, due to the low MCA and sizeable magnetostriction of NiO, and high spin Hall angle of Pt. The Neél vector read-out mechanism was verified first, by providing a novel measurement of both angle and magnetic field-resolved SMR in a non-crystalline material. The writing mechanism was examined next by measuring an increased uniaxial SMR amplitude when larger tensile strains were applied to the sample. Small biaxial tensile strains of 250 με were observed to be sufficient to produce 52% modification of the SMR at 11 T, indicating a high sensitivity of antiferromagnetic domain structure to strain. In addition, the changing SMR was observed to be linear in the small strain regime, perhaps implying a linear theory of magnetostriction for antiferromagnets similar to that for

ferromagnets. This work is intended to motivate further research into (i) magnetostrictive antiferromagnets with low intrinsic anisotropy, and (ii) mechanisms for quantifying the induced magnetostrictive anisotropy in strained antiferromagnets. It also clarifies that strain control of antiferromagnets for Néel vector switching-operated memory is feasible, and may preserve the energy efficiency benefits of multiferroics as observed in ferromagnets. The fact that the magnetoelastic anisotropy potentially dominates the antiferromagnetic domain structure may be a help, not a hindrance, to antiferromagnetic memory control.

5.5. Chapter References

[1] Nakayama, H., et al. "Spin Hall magnetoresistance induced by a nonequilibrium proximity effect." *Physical review letters*110.20 (2013): 206601.

[2] Sapozhnik, A. A., et al. "Direct imaging of antiferromagnetic domains in Mn 2 Au manipulated by high magnetic fields." *Physical Review B* 97.13 (2018): 134429.

[3] Bodnar, S. Yu, et al. "Writing and reading antiferromagnetic Mn 2 Au by Néel spin-orbit torques and large anisotropic magnetoresistance." *Nature communications* 9.1 (2018): 348.

[4] Němec, Petr, et al. "Antiferromagnetic opto-spintronics." *Nature Physics* 14.3 (2018): 229.

[5] Wang, K. L., J. G. Alzate, and P. Khalili Amiri. "Low-power non-volatile spintronic memory: STT-RAM and beyond." *Journal of Physics D: Applied Physics* 46.7 (2013): 074003.

[6] Baldrati, Lorenzo, et al. "Full angular dependence of the spin Hall and ordinary magnetoresistance in epitaxial antiferromagnetic NiO (001)/Pt thin films." *Physical Review B*98.2 (2018): 024422.

[7] Alberts, L., and E. W. Lee. "Magnetostriction in antiferromagnetic nickel oxide." *Proceedings of the Physical Society* 78.5 (1961): 728.

[8] Roth, W. L. "Magnetic structures of MnO, FeO, CoO, and NiO." *Physical Review* 110.6 (1958): 1333.

[9] Grössinger, R. "Correlation between the inhomogeneity and the magnetic anisotropy in polycrystalline ferromagnetic materials." *Journal of Magnetism and Magnetic Materials*28.1-2 (1982): 137-142.

[10] Bozorth, R. M. "Determination of ferromagnetic anisotropy in single crystals and in polycrystalline sheets." *Physical Review*50.11 (1936): 1076.

[11] Belov, K. P., and R. Z. Levitin. "MAGNETOSTRICTION OF ANTIFERRO-MAGNETIC NICKEL MONOXIDE." *SOVIET PHYSICS JETP-USSR* 10.2 (1960): 400-401.

[12] Domann, John P., et al. "Strain-mediated multiferroic control of spontaneous exchange bias in Ni-NiO heterostructures." *Journal of Applied Physics* 120.14 (2016): 143904.

[13] Baldrati, Lorenzo, et al. "Full angular dependence of the spin Hall and ordinary magnetoresistance in epitaxial antiferromagnetic NiO (001)/Pt thin films." *Physical Review B*98.2 (2018): 024422.

[14] Schmid, P., et al. "Gauge factor of titanium/platinum thin films up to 350 C." *Procedia Engineering* 87 (2014): 172-175.

[15] Wrbanek, J., et al. "A thin film multifunction sensor for harsh environments." *37th Joint Propulsion Conference and Exhibit*. 2001.

[16] Liu, Jun, et al. "Correlation between the spin Hall angle and the structural phases of early 5 d transition metals." *Applied Physics Letters* 107.23 (2015): 232408.

[17] Hoogeboom, Geert R., et al. "Negative spin Hall magnetoresistance of Pt on the bulk easy-plane antiferromagnet NiO." *Applied Physics Letters* 111.5 (2017): 052409.

[18] Weber, N. B., et al. "Magnetostrictive domain walls in antiferromagnetic NiO." *Physical review letters* 91.23 (2003): 237205.

[19] O'handley, Robert C. *Modern magnetic materials: principles and applications*. Wiley, 2000.

VI. Conclusion

This dissertation proposes improving the speed and energy efficiency of magnetic memory by changing the types of materials that are used. Specifically, common ferromagnetic materials (CoFeB, for example) can be replaced by multilayers or antiferromagnetic alternatives, with antiferromagnets offering larger improvements but also more difficult integration. To enable the use of these new materials, this dissertation identifies and solves three critical shortcomings in the magnetic physics literature:

(i) While multilayers are commonly used in magnetic memory, little work has been done to enable device-level modeling of multilayers. This means that the crucial interlayer coupling, which dictates the behavior of the entire composite in most cases, cannot purposefully be designed to meet desired device performance metrics. To overcome this problem, this dissertation develops a new micromagnetic modeling approach that includes the "usual" micromagnetic dynamics in each layer, an additional interlayer exchange coupling term, and accounts for the exponential decay of the interlayer coupling away from the interface. The predictions of the new model and MuMax3, a publicly available micromagnetics solver, were compared to magnetic depth profiles obtained by neutron scattering. The new model was observed to over-estimate magnetic gradients compared to MuMax3, which tends to under-estimate them. Using both solvers together allows for simultaneous estimation of the upper- and lower-bounds of magnetic gradients in multilayer stacks, a metric that was not possible to estimate previously.

(ii) Antiferromagnets, which are of interest for their THz switching speeds, are not currently possible to integrate into magnetic memory because there is no known on-

chip switching mechanism and also no way to model the device-level micromagnetic dynamics. This dissertation solves both of these issues by first proposing voltage-controlled piezostrains as a control mechanism, and then developing a new micromagnetic model that includes the fully-coupled magneto-electro-mechanical dynamics. The model was then tested using prototypical material properties, which confirmed the possibility of strain-swtiching at high speed (above 10 GHz) and low power (~50 aJ/state switch). The model also elucidated unique features of strain-coupled antiferromagnets regarding shape and symmetry. This modeling approach is generalizable to most antiferromagnets and thus provides a new guideline for antiferromagnet-multiferroic design.

(iii) In addition to improving the micromagnetic modeling of antiferromagnets, this dissertation also proves the first feasibility test for mutliferroic switching of antiferromagnets via small strains in the linear piezoelectric regime. The experiment analyzed Néel vector rotation in a candidate NiO/Pt Hall bar during voltage-controlled strain-mediated anisotropy changes, with spin Hall magnetoresistance as a read-out mechanism. In particular, changes in the composite's strain state were observed to increase its magnetoresistance at a given magnetic field, implying a propotional change in the magnetic susceptibility. The strain change in susceptibility when 200 V was applied across the mutliferroic's PMN-PT was seen to be similar to that observed under an additional 3 Tesla of externally applied magnetic field. The magnetoresistance also seemed to scale linearly with strain, implying a linear strain-to-anisotropy relation in antiferromagnets, similar to that observed in ferromagnets. This was a first-ever estimation of the antisotropy present in strained antiferromagnets.

The author hopes that the advancements listed here will aid in interpreting experimental data about mutlilayers and antiferromagnets by providing new modeling techniques and proof-of-concept experiments. The outlook for magnetic memory based on either multilayers or antiferromagnets is promising, but significant materials research is still needed. Regarding multilayers, author also hopes that further investigation will be done regarding low-intrinsic anisotropy antiferromagnets with high magnetostriction, and optimization of device geometry for strain-controlled antiferromagnetic memory.